

Steplike electric conduction in a classical  
two-dimensional electron system through a narrow  
constriction in a microchannel

Moto Araki



## Acknowledgments

Foremost, I would like to acknowledge my PhD supervisor, Professor Hisao Hayakawa in Kyoto University for providing me with the opportunity to complete my PhD thesis. I really appreciate his advice, encouraging, and constructive feedback he gave me. Besides my supervisor, I am grateful to Associate Professor Takeaki Araki in Kyoto University for his insightful advice on my research. I want to thank all members of Professor Hayakawa's group for their fruitful comments on research. I also thank all staffs of Yukawa Institute for Theoretical Physics (YITP) and Division of Physics and Astronomy, Graduate School of Science, Kyoto University for their kindness.

I thank Professor Kimitoshi Kono and Doctor David Rees in RIKEN for fruitful discussions on their experiment. Without their help, my research would not have been possible.

This work was partially supported by the Ministry of Education, Culture, Science and Technology (MEXT), Japan (Grant No. 21540384), and by the Global COE program, The Next Generation of Physics, Spun from Universality and Emergence, from MEXT Japan. The author also thanks the Yukawa International Program for Quark-Hadron Sciences at Yukawa Institute for Theoretical Physics, Kyoto University. The numerical calculations were carried out on the SR16000 and Altix3700 BX2 at YITP in Kyoto University.

Finally, I thank my parents for their faith and support.

# Abstract

Using molecular dynamics simulations, we investigate transport properties of classical two-dimensional electrons through a microchannel with a narrow constriction. The electrons are confined by and interact with each other through electric potential derived from the Poisson equation under boundary conditions to imitate a device structure in a recent experiment [D. G. Rees *et al.*, Phys. Rev. Lett. **106**, 026803 (2011)]. The electron system of our simulation is a realistic model for strongly correlated electrons on liquid helium in the microscale device. In the simulations, the electrons are driven by the chemical potential difference between two particle baths. As a function of the confinement strength of the constriction, the calculated conductance in the simulations exhibits steplike increases as reported in the experiment. It is confirmed that the number of the steps corresponds to the number of stream lines formed by the flow of self-organizing distributed electrons at the constriction. For the strong confinement, the conductance is affected by the temporal potential fluctuation which induces intermittent disappearances of a potential barrier to exist in the constriction. We also observe the temporal change of the number of electrons to pass through the constriction, which may be due to short-wavelength density fluctuations. Therefore, we suppose that the change of the stream lines, forced by the strong electron correlation and the change of the confinement strength, causes the steplike behavior in the conductance, and the density fluctuation plays a certain role in smoothing the steps.

# Contents

<b>1</b>	<b>Introduction</b>	<b>7</b>
1.1	Transport in confined geometry . . . . .	7
1.2	Many-particle transport in confined geometry . . . . .	8
1.3	Steplike electric conduction in strongly correlated electrons on liquid helium . . . . .	8
1.4	Overview of this thesis . . . . .	8
1.5	Organization of this thesis . . . . .	9
<b>2</b>	<b>Model, and Numerical Methods</b>	<b>11</b>
2.1	Electron states and transport properties in the confined electron system over liquid $^4\text{He}$ on metal electrodes . . . . .	11
2.2	Interaction and confining potentials . . . . .	12
2.3	Constant temperature and chemical potential molecular dynamics . . . . .	13
2.4	Simulation setup . . . . .	16
2.5	Conductance calculation . . . . .	17
<b>3</b>	<b>Results of the simulations</b>	<b>19</b>
<b>4</b>	<b>Discussion</b>	<b>25</b>
4.1	Density-fluctuation-affected transport properties . . . . .	25
4.2	Comparison of our result with the observed conductance . . . . .	28
4.3	Langevin dynamics simulation . . . . .	30
<b>5</b>	<b>Conclusion</b>	<b>33</b>
<b>A</b>	<b>Electric potential, quantized electron states, and classical 2D Hamiltonian</b>	<b>35</b>
A.1	Derivation of electric potential . . . . .	35
A.2	Evaluation of the screening effect due to the existence of liquid $^4\text{He}$ . . . . .	38
A.3	Quantized electron states in the vertical direction against the liquid surface and effective 2D Hamiltonian . . . . .	39
A.4	Regarding of the difference between our model and the device structure . . . . .	45

<b>B</b>	<b>2D electron transport over liquid <math>^4\text{He}</math> in idealized geometry</b>	<b>47</b>
B.1	Bulk 2D electron transport over liquid $^4\text{He}$ on metal electrodes . . . .	47
B.2	Estimation of conductance for the electrons in idealized channel geometry	50
<b>C</b>	<b>Details on molecular dynamics simulation method</b>	<b>53</b>
C.1	Reason to select constant temperature and chemical potential molecular dynamics . . . . .	53
C.2	New grand canonical ensemble molecular dynamics . . . . .	57
<b>D</b>	<b>Conductance under the various parameters</b>	<b>61</b>
<b>E</b>	<b>Calculation method of physical quantities</b>	<b>67</b>
<b>F</b>	<b>Fluctuation properties</b>	<b>69</b>

# Chapter 1

## Introduction

### 1.1 Transport in confined geometry

Electric conduction in confined geometry has been an important subject of study to characterize properties in the mesoscopic scale [1], and its study has a wide possibility of applications to electronics [2, 3]. Transport properties in confined geometry are roughly determined by the scale of geometry,  $W$ , the mean free path  $l_m$ , the de Broglie wavelength  $\lambda_D$ , and the phase-relaxation length  $l_\varphi$  [1, 4]. Here,  $W$  is, for example, the width of channel geometry or the separation of a point contact, and  $l_\varphi$  is the average distance in which the quantum-mechanical phase of the carrier is randomized by inelastic scattering.

From these characteristic lengths, the transport can be classified whether dynamics is classical ( $W \gg \lambda_D$  and  $l_m > l_\varphi$ ) or quantum, and transport is ballistic ( $l_m \gg W$ ) or diffusive ( $l_m \ll W$ ) [4–11]. In the classical diffusive transport to show ohmic behavior, the geometrical effects in point-contact geometry was studied firstly by Maxwell [12]. In the quantum diffusive region, quantum interference effects such as electron localization or universal conductance fluctuations is may observed in transport [4]. On the other hand, Sharvin studied electron transport in point-contact geometry in the classical ballistic region, and shows the existence of non-zero resistance in the system without scatterers [13–15]. Under the condition  $W \approx \lambda_D$  in the ballistic region, quantum size effects is observed, in which conductance quantization in two-dimensional (2D) electron gas confined in point-contact geometry is well known [1, 16, 17].

To understanding clearly these transport properties, correlation effects between electrons are also important, and investigated mainly with kinetic approaches which are the framework for rarefied gas [4, 18–22]. However, the object we study is one of strongly correlated electron systems, and so it is not clear whether the transport in the systems can be discussed in the above classification.

## 1.2 Many-particle transport in confined geometry

Transport for inhomogeneous dense liquids in which the exclusion effects between particles are important has been studied only experimentally and computationally because of theoretical difficulties. As strong correlation effects to affect the transport, layers formed by colloidal particles in channel geometry [23,24], pinning and depinning at a constriction [25], and anisotropic and non-uniform mobility in thin film geometry between two parallel planar boundaries [26–28] are observed.

## 1.3 Steplike electric conduction in strongly correlated electrons on liquid helium

Recently, Rees *et al.* have found the existence of steplike conductance in the conduction of classical 2D electrons on liquid  $^4\text{He}$  (Refs. [29] and [30]) using a device with point-contact geometry [31]. For the 2D electrons on liquid  $^4\text{He}$  known as a strongly correlated classical electron system, they have measured the conductance at the various confinement strengths of the contact. The conductance and the corresponding derivative show, respectively, steplike increase and characteristic oscillation as the strength is weakened (Fig. 1.1). They suggest that the origins of the conductance are not quantum effects, as in the conductance quantization [16], but are attributed to the increment of the number of electrons that can pass simultaneously through the constriction. We find it necessary to justify their suggestion and to clarify the mechanisms of the dynamics behind the steplike conduction of electrons on liquid  $^4\text{He}$ . The main goal of this paper, thus, is to understand the mechanisms of the steplike conduction in classical 2D electron systems, and investigate transport properties of strongly correlated classical electron systems in confined geometry

## 1.4 Overview of this thesis

In this paper, we investigate the electric conduction of the classical 2D electron system through a narrow constriction in a microchannel using a molecular dynamics (MD) simulation with two particle baths under a Nosé-Hoover thermostat. The electrons in the MD simulations are confined in a point-contact-like shape and interact with each other, in terms of electric potential derived from the Poisson equation under a boundary condition given so as to imitate the device in Ref. [31] (see Fig. 2.1). Our model and method stand on the presumption that the many-body effects in the confined geometry are essential for the steplike electric conduction (see Sec. 2.1 and Appendix B). We calculate conductance as a function of the confinement strength of the constriction. To confirm the suggestion by Rees *et al.* [31] and to develop the understanding of the steplike conduction, we investigate the static and dynamical properties of electrons near the constriction from the spatial distribution of electron density, electrostatic potential, and potential fluctuation.

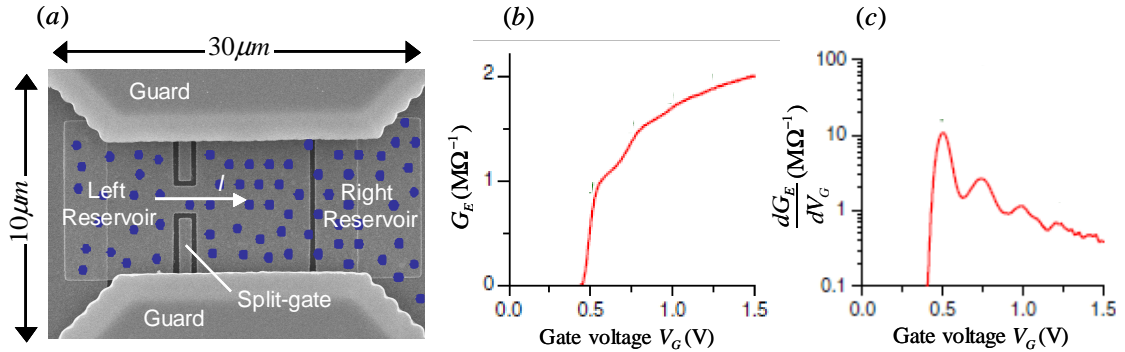


Figure 1.1: (a) The device structure in the experiment, taken from [31]. The device consists of the guard, split-gate, left reservoir, and right reservoir electrodes, in which the region of the reservoir electrodes is filled with liquid  $^4\text{He}$ . The lower voltage than the reservoir electrodes is applied to the guard electrodes, thereby the electrons are confined in channel geometry, and the gate voltage  $V_G$  is applied to the split-gate electrodes. (b) The measured conductance  $G_E$  in the experiment vs the gate voltage  $V_G$ , taken from [31]. (c) The corresponding derivative  $dG_E/dV_G$  vs the gate voltage  $V_G$ , taken from [31].

This paper is also closely related to the molecular dynamics simulation for non-charged particles through a bottleneck, driven by an external force [32]. The present paper can be regarded as a realistic version of their model.

## 1.5 Organization of this thesis

The organization of the paper is as follows. In Chapter 2, our model, methods, and simulation details are provided. The conductance and the other quantities calculated in our simulations are presented in Chapter 3, in which the suggestion by Rees *et al.* [31] is also verified. Based on the results of our simulations in Chapter 3, we discuss the mechanisms causing the observed conductance in Sec. 4.1. In Sec. 4.2, we compare our results with the observed conductance in the experiment. We also present the result of the Langevin dynamics (LD) simulation method which is the molecular dynamics using the Langevin thermostat in Sec. 4.3. The results and the discussions are summarized in Chapter 5. In appendices, we present some detailed descriptions of our model and method. In Appendix A, we derive electric potential for the 2D electron system over liquid  $^4\text{He}$  on metal electrodes in the confined geometry, and introduce Hamiltonian which reduces classical 2D Hamiltonian on the liquid surface for strongly correlated electrons. In Appendix B, we calculate the conductance for the scattered electrons by helium vapor atoms and ripples in idealized geometry. In Appendix C, the details on molecular dynamics simulation method is described, where the comparison of the driving field we adopt with that for the experiment is performed [31]. In Appendix D, we show the obtained conductance from the simulations for the various parameters. In Appendix E, we give the details of the

method to calculate physical quantities. In Appendix F, we investigate fluctuation dynamics in our MD simulations, and compare it with previous studies.

# Chapter 2

## Model, and Numerical Methods

In this chapter, we introduce our model with a demonstration to justify our treatment for the electrons in the device in Ref. [31] and explain the method of the MD, including how to provide the simulation setup and to calculate observed quantities.

### 2.1 Electron states and transport properties in the confined electron system over liquid ${}^4\text{He}$ on metal electrodes

In this section, we briefly explain the electron state and the transport process of electrons in the device in Ref. [31]. The former and the latter are described in detail in Appendix A and B, respectively.

The system of electrons over liquid  ${}^4\text{He}$  on metal electrodes studied by Rees *et al.* [31] is an ideal system to investigate strongly correlated classical 2D electron systems [28–31, 33, 34]. The electrons are excluded at the liquid surface, and interact polarized liquid  ${}^4\text{He}$  and charges induced in the metal electrodes [35]. We also apply a holding electric field  $E_{\perp}$  normal to the liquid surface. For surface density  $n_s \sim 10^8 - 10^9 \text{cm}^{-2}$ , temperature  $T \sim 1$  K, and liquid thickness  $z_{\text{He}} \sim 1 \mu\text{m}$ , the inter-electron separation,  $r_s = 2/\sqrt{\pi n_s} \sim 10^{-1} \mu\text{m}$ , is much larger than the thermal de Broglie wavelength,  $\lambda_D \sim 10^{-2} \mu\text{m}$ , and the energy gap between the ground and the first excited state,  $\Delta \sim 19$  K, is sufficiently larger than the temperature [36]. Hence, the electrons occupy the ground state of the independent quantum states for the vertical motion, whereas the parallel motion in the 2D plane at the position of the ground state is classical.

For the bulk 2D electrons, it is known that the mobility on the surface is little affected by the scatterings by roughness on the interface liquid substrate for  $z_{\text{He}} \sim 1 \mu\text{m}$  [37–40], but is dominated by the scatterings between electrons and helium gas atoms for  $T > 1$  K or between electrons and ripplons at lower temperature [28, 29, 35, 41]. The correlation effects between electrons on the transport have been discussed by the kinetic equation method under the complete control approximation [42–46],

the force-balance method [40, 47, 48], and more sophisticated theory [29, 49, 50].

In confined geometry, the classical transport is roughly classified into the ballistic and the diffusive region [5–11]. For the transport in the ballistic region, we need to calculate directly the observed macroscopic transport coefficients from microscopic theories. In the diffusive region, we can approximately separate the dynamics into macroscopic and microscopic process for the transport relaxation realized within much smaller spatial extent than the scale of geometry,  $W$ .

In Appendix B, we briefly estimate the conductance for the 2D electron system over liquid  $^4\text{He}$  on metal electrodes in idealized channel geometry of the device structure in Ref. [31]. The result supports that the many-body effects in the confined geometry are dominant for the steplike electric conduction.

## 2.2 Interaction and confining potentials

In this section, we present the forms of interaction potential between electrons and confining potential for our MD (see Appendix A for more detail). The electric potential energy for the  $i$ -th electron on liquid  $^4\text{He}$  is given by [52]

$$\phi(\mathbf{r}_i, t) = \sum_{j(\neq i)} \phi_{\text{I}}[r_{ij}(t)] + \phi_{\text{C}}[\mathbf{r}_i(t)], \quad (2.1)$$

where  $\mathbf{r}_i(t) = [x_i(t), y_i(t)]$  is the position of the  $i$ -th electron at  $z = z_h$  at time  $t$ ,  $r_{ij}(t) \equiv |\mathbf{r}_i(t) - \mathbf{r}_j(t)|$ ,  $\phi_{\text{I}}(r)$  is the interaction potential energy between two surface electrons, and  $\phi_{\text{C}}(\mathbf{r})$  is the confining potential energy. We solve the three-dimensional (3D) Poisson equation for  $\phi$  in the semi-infinite domain  $z \geq 0$ , and presume the electrons to be confined at the height  $z = z_h$  from the plane  $z = 0$ , where this

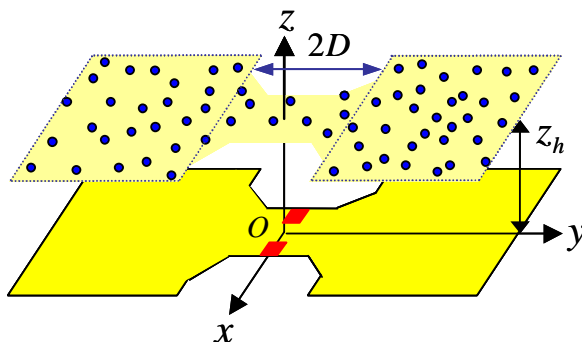


Figure 2.1: A schematic view of our simulation setup of a classical 2D electron system confined on the plane at  $z = z_h$ , taken from [51]. On the boundary plane  $z = 0$ , the yellow region and the red regions, respectively, correspond to the reservoir electrode and the split-gate electrodes in the experiment [31]. The system consists of a left and a right reservoirs, and a channel of length  $2D$ , where the reservoirs are connected with the channel.

treatment is justified in Appendix A. Here, we set  $z_h$  as the thickness of liquid  $^4\text{He}$ ,  $z_h = 1.5 \mu\text{m}$ , which follows the experimental setup [31] (Fig. 2.1). Therefore, the potential is obtained from an analytic solution at  $z = z_h$  of the Poisson equation. Then,  $\phi_I(r)$  is given by [53, 54]

$$\phi_I(r) = e^2 \left[ \frac{1}{r} - \frac{1}{\sqrt{r^2 + 4z_h^2}} \right], \quad (2.2)$$

where  $e$  is the elementary electric charge. The right-hand side in Eq. (2.2) consists of the bare Coulomb interaction and the dominant screening effects between surface electrons which represents the contribution of the image charge induced in the metal electrodes (see Appendix A.1).

The boundary conditions we impose on the Poisson equation are

$$\phi(\mathbf{r}, z = 0) = \begin{cases} V_0 & (\mathbf{r} \in S_0) \\ V_G & (\mathbf{r} \in S_G) \\ 0 & (\mathbf{r} \notin S_0 \cup S_G) \end{cases} \quad (2.3)$$

and

$$\phi(\mathbf{r}, z) = 0 \quad (|\mathbf{r}| \text{ or } z \rightarrow \infty) \quad (2.4)$$

where  $S_0$ ,  $S_G$ , and the outside of  $S_0 \cup S_G$  at  $z = 0$ , respectively, represent the reservoir, the split gate, and the guard electrodes [31] [see Fig. 2.2(a)]. Then,  $\phi_C(\mathbf{r})$  is represented as

$$\begin{aligned} \phi_C(\mathbf{r}) = & -\frac{eV_0}{4\pi} \int_{S_0} dx_0 dy_0 \left[ \frac{2z_h}{[|\mathbf{r} - \mathbf{r}_0|^2 + z_h^2]^{3/2}} \right] \\ & -\frac{eV_G}{4\pi} \int_{S_G} dx_0 dy_0 \left[ \frac{2z_h}{[|\mathbf{r} - \mathbf{r}_0|^2 + z_h^2]^{3/2}} \right], \end{aligned} \quad (2.5)$$

where  $V_0$  and  $V_G$  are the voltages of a reservoir and a split-gate, respectively. It should be noted that each integration in Eq. (2.5) can be performed exactly if we assume that the integration range consists of rectangles and triangles, as in Fig. 2.2(a) (see Appendix A.3).

We also adopt  $V_0 = 0.38 \text{ V}$  and  $V_G$  of the range from  $-0.05 \text{ V}$  to  $0.38 \text{ V}$ , which imitates the device in Ref. [31]. When  $V_G$  is set to  $V_0$ ,  $\phi_C$  works as the confinement without the point contact, and when  $V_G$  is set to a voltage lower than  $V_0$ ,  $\phi_C$  additionally generates the point contact due to a voltage induced between  $S_0$  and  $S_G$ , as seen in Figs. 2.2(b) and (c).

## 2.3 Constant temperature and chemical potential molecular dynamics

Our MD is built on a hybrid scheme of a constant temperature MD (CTMD) with a Nosé-Hoover thermostat [55–57] and a constant chemical potential MD (CCMD)

[58–61]. The reason we adopt the Nosé-Hoover thermostat is as follows: This method is the established one to reproduce the precise equilibrium state, and the equation of motion for electrons can keep the local time-reversal symmetry (see Appendix C.1). In CCMD, we introduce a fractional particle characterized by an extended number variable (ENV) for a particle bath, where the integer part of the ENV denotes the number of particles, and the fractional part represents the value of the fractional particle. The ENV couples with the system through the fractional particle interacting with the rest of the system.

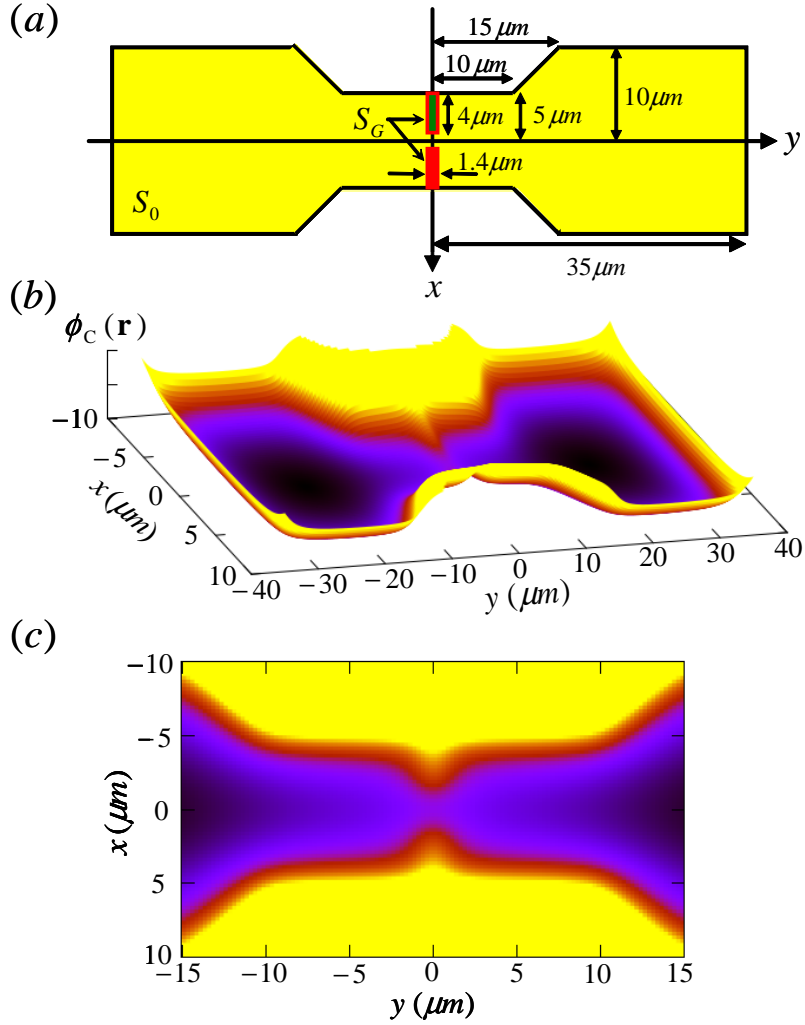


Figure 2.2: (a) The boundary condition at  $z = 0$ :  $S_0$  and  $S_G$ , respectively, are the yellow and red regions, taken from [51]. The electric potential in  $S_0$  and the outside of the colored regions are  $V_0$  and  $0$ , respectively. The gate voltage  $V_G$  is imposed to  $S_G$ . (b) The confining potential energy  $\phi_C$  for  $V_0 = 0.38$  V,  $V_G = 0.38$  V, and  $z_h = 1.5\ \mu\text{m}$  in Eq. (2.5), taken from [51]. (c) The contour plot of  $\phi_C$  in the channel, which is the region of  $|y| < D = 15\ \mu\text{m}$ , taken from [51].

In our simulation, the system consists of a left and a right reservoir, and a channel of length  $2D$  with  $D = 15 \text{ } \mu\text{m}$ , where the reservoirs are connected with the channel (see Figs. 2.1 and 2.2). The left (right) reservoir has an electrochemical potential  $\mu_L$  ( $\mu_R$ ) which can be divided into two parts as,

$$\mu_\gamma = \mu_\gamma^0 + \mu_\gamma^1, \quad (2.6)$$

with  $\gamma = L, R$ , where  $\mu_\gamma^0$  is the intrinsic part of the ideal chemical potential [62], and  $\mu_\gamma^1$ , which is the control parameter in our MD, is the sum of the excess chemical potential and the confining potential energy. The left (right) reservoir consists of one fractional particle and temporally variational  $N_L$  ( $N_R$ ) electrons in  $S_L$  ( $S_R$ ), where  $S_L$  ( $S_R$ ) is the region  $y < -H$  ( $y > H$ ) with  $H = 15 \text{ } \mu\text{m}$  (see Fig. 2.3).

The equation of motion for the electrons in our MD is given by

$$m \frac{d^2 r_i^\alpha}{dt^2} = -\frac{\partial \phi(\mathbf{r}_i)}{\partial r_i^\alpha} - m \dot{\zeta} \dot{r}_i^\alpha - \theta(-y_i - H) [\nu_L - N_L] \frac{\partial \phi_I(r_{iL})}{\partial r_i^\alpha} - \theta(y_i - H) [\nu_R - N_R] \frac{\partial \phi_I(r_{iR})}{\partial r_i^\alpha}, \quad (2.7)$$

where  $r_i^\alpha$  and  $r_{L(R)}^\alpha$  are, respectively, the  $\alpha$  component ( $\alpha = x, y$ ) of the position of the  $i$ -th electron and the fractional particle belonging to the left (right) reservoir,  $r_{iL(R)} \equiv |\mathbf{r}_i - \mathbf{r}_{L(R)}|$ ,  $\nu_L$  ( $\nu_R$ ) is the ENV of the left (right) reservoir,  $m$  is the electron mass, and  $\theta(x)$  is a step function, i.e.,  $\theta(x) = 1$  for  $x > 0$ , and  $\theta(x) = 0$  otherwise. Here, the ‘‘friction’’ coefficient  $\zeta$  is adjusted according to the following equation [57]:

$$Q_\zeta \frac{d^2 \zeta}{dt^2} = 2 \left[ \sum_i \frac{m \dot{r}_i^2}{2} - N k_B T_K \right], \quad (2.8)$$

where  $Q_\zeta$  is the ‘‘mass parameter’’ of  $\zeta$ ,  $N$  is the temporally variational total number of electrons,  $k_B$  is the Boltzmann constant, and  $T_K$  is the expected kinetic temperature. The time evolutions of the fractional particle coordinate  $r_\gamma^\alpha$  and the ENV  $\nu_\gamma$  are respectively given by

$$m \frac{d^2 r_\gamma^\alpha}{dt^2} = -(\nu_\gamma - N_\gamma) \left[ \sum_{i \in S_\gamma} \frac{\partial \phi_I(r_{\gamma i})}{\partial r_\gamma^\alpha} + \frac{\partial \phi_C(\mathbf{r}_\gamma)}{\partial r_\gamma^\alpha} \right], \quad (2.9)$$

$$Q_\nu \frac{d^2 \nu_\gamma}{dt^2} = \mu_\gamma^1 - \left[ \sum_{i \in S_\gamma} \phi_I(r_{\gamma i}) + \phi_C(\mathbf{r}_\gamma) \right], \quad (2.10)$$

where  $Q_\nu$  is the mass parameter of  $\nu_\gamma$ .

The temporal variations of  $N_L$  and  $N_R$  are governed by the following protocol [61]. When  $\nu_\gamma - N_\gamma$  becomes zero, we delete the fractional particle, and replace one electron in the reservoir by a new fractional particle satisfying  $\dot{\nu}_\gamma^{\text{old}} = \dot{\nu}_\gamma^{\text{new}}$ , when the coordinate

and the velocity for the deleted fractional particle are discarded, and those of the replaced electron are given over to the new fractional particle. When  $\nu_\gamma - N_\gamma$  becomes one, we convert the fractional particle into an electron, and insert a new fractional particle at the position where the fractional particle satisfies  $\ddot{\nu}_\gamma^{\text{old}} = \ddot{\nu}_\gamma^{\text{new}}$  and the potential energy also satisfies a local minimum condition  $\ddot{\mathbf{r}}_\gamma \simeq 0$ , when the coordinate and the velocity of the converted fractional particle are given over to the new electron, and the velocity of the new fractional particle is set to zero. The condition  $\ddot{\nu}_\gamma^{\text{old}} = \ddot{\nu}_\gamma^{\text{new}}$  ensures the temporal continuity of  $\ddot{\nu}_\gamma$ , and  $\ddot{\mathbf{r}}_\gamma \simeq 0$  works so as not to change the average velocity of the system due to the insertions of a fractional particle. Moreover, the inserting place of the fractional particle in the left (right) reservoir is selected from the squares created by dividing area  $A_L$  ( $A_R$ ) in  $S_L$  ( $S_R$ ) into  $0.01 \mu\text{m}$  square mesh, based on the condition described above (see Fig. 2.3). The behavior of electrons in the channel is not disturbed by the fractional particles, because if the fractional particles try to enter the channel,  $\ddot{\nu}_\gamma$  increases, and thus the fractional particle is converted into an electron according to the above protocol for the particle conversion.

## 2.4 Simulation setup

Throughout our MD simulations the initial total number of electrons  $N_I$  is 1284, and the initial positions of electrons are located in the ground-state configuration which forms a classical 2D Wigner crystal deformed by the confinement at each  $V_G$ . The initial velocities of electrons are randomly assigned from the Maxwell-Boltzmann distribution at  $T_K = 1.2$  K corresponding to the experimental setup [31]. The initial positions of the fractional particles are determined based on the protocol in the case of  $\ddot{\nu}_\gamma = 0$ , and their initial velocities are set to zero,  $\dot{\mathbf{r}}_\gamma = 0$ . The extension variables are initially set to:  $\nu_\gamma = N_\gamma + 0.5$ ,  $\dot{\nu}_\gamma = 0$ ,  $\zeta = 0$ , and  $\dot{\zeta} = 0$ .

We choose  $Q_\zeta$  as:  $Q_\zeta = k_B T_K N_I \tau_N^2 = 6.02 \times 10^{-20} \text{ meV}\cdot\text{s}^2$ , where  $\tau_N = 2.13 \times 10^{-11}$

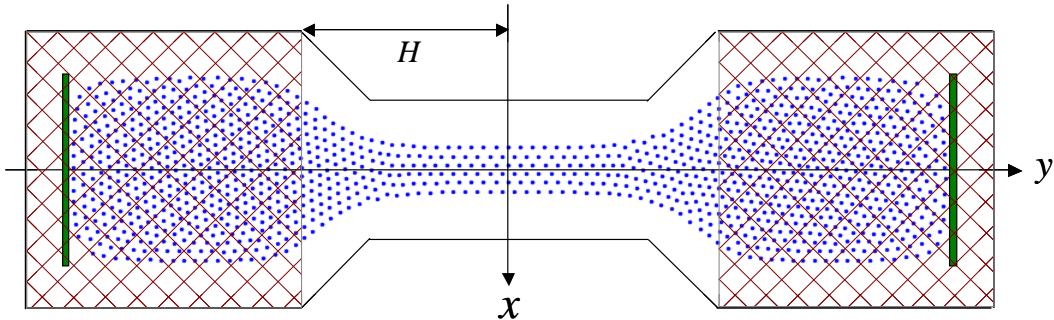


Figure 2.3: A schematic view for the range  $S_L$  ( $S_R$ ) of interaction of the fractional particles with electrons in the left (right) reservoir (cross-hatched regions), and the insertion area  $A_L$  ( $A_R$ ) of the fractional particle in the left (right) reservoir (green areas). Here, the blue circles indicate the position of electrons in the ground-state configuration for  $V_G = 0.38$  V, and  $\mu_L = \mu_R = 48.96$  meV.

is the Nosé-Hoover relaxation time. The value of  $\tau_N$  is to make the thermostat work effectively [63], and is close to the characteristic period of short-wavelength vibrations of the bulk 2D Wigner crystal [64],  $\tau_s = 8.52 \times 10^{-11}$  s. It is believed that the temporal variation of temperature does not affect long-wavelength conductivity directly because the temperature fluctuation induces only short-wavelength fluctuations in the momentum of electrons. We also carry out the MD simulations with another mass parameter  $Q'_\zeta = 16Q_\zeta$ , and then obtain quantitatively similar results for all quantities calculated in the following. Although it is known that  $Q_\nu$  affects the cycle of fluctuation in the number of particles, we use one parameter  $Q_\nu = E_0 t_0^2$  with  $E_0 = 1.44$  meV and  $t_0 = 6.28 \times 10^{-11}$  s which are our MD units of energy and time, respectively, and verify that time-averaged quantities are unchangeable for  $10Q_\nu$  and  $0.1Q_\nu$ . Because of the restriction of our computer resources, we have to limit the insertion areas  $A_L$  and  $A_R$  to the regions

$$\begin{aligned} A_L &= \{(x, y) \mid -y_{\max} \leq y \leq -y_{\min}, |x| \leq x_{\max}\} \\ A_R &= \{(x, y) \mid y_{\min} \leq y \leq y_{\max}, |x| \leq x_{\max}\} \end{aligned}$$

with  $y_{\min} = 31.7 \mu\text{m}$ ,  $y_{\max} = 32.2 \mu\text{m}$ , and  $x_{\max} = 7 \mu\text{m}$ , where  $-y_{\min}$  ( $y_{\min}$ ) corresponds to the average position of the electron present at the furthest left (right) in all of the electrons in the left (right) reservoir (see Fig. 2.3).

We fix  $\mu_L^1$  and  $\mu_R^1$  as  $\mu_L^1 = 49.16$  meV and  $\mu_R^1 = 48.96$  meV, where we set the minimum of the confining potential energy to zero. Thus the chemical-potential difference  $\Delta\mu^1 \equiv \mu_L^1 - \mu_R^1$  induces a direct current (dc) between the reservoirs. The difference of the driving field between our system and the experiment [31] is discussed in Appendix C.1. We also confirm the linearity of the current in  $\Delta\mu^1$  (see Fig. D.1 in Appendix D). For the  $\mu_\gamma^1$  we set, the electron density  $\bar{n} = 4/\pi\bar{r}^2$  in the channel is  $\bar{n} \approx 2.2 \times 10^8 \text{ cm}^{-2}$  for  $V_G = 0.38$  V, where  $\bar{r} \approx 0.77 \mu\text{m}$  is the inter-electron separation in the channel. Thereby, the 2D electrons belong to a liquid state for the bulk system [65] because the plasma parameter  $\Gamma = e^2\sqrt{\pi\bar{n}}/k_B T_K \approx 37$  is much smaller than the critical plasma parameter  $\Gamma_c = 137$  [66].

## 2.5 Conductance calculation

Under the above setup, we calculate the electric current, density distribution, potential energy, fluctuation of potential energy, etc. in a steady state after 500,000 steps from the initial state (see Appendix E for details). In order to obtain the conductance

$$G(V_G) = -eI(V_G)/\Delta\mu, \quad (2.11)$$

as a function of  $V_G$ , we compute the electric current in the  $y$  direction in the channel at each  $V_G$ ,

$$I(V_G) = -e \frac{\langle \sum_i \theta [D - |y_i(t)|] \dot{y}_i(t) \rangle}{2D}, \quad (2.12)$$

under the assumption  $\Delta\mu = \Delta\mu^1$ . In this paper,  $\langle \cdots \rangle$  represents both the ensemble and the time averages, where the ensemble is generated with the different random seeds for the initial velocity distribution. Through the current calculation, it is confirmed that the replacement of  $D$  in Eq. (2.12) by  $y_{\min}$  or  $y_{\max}$  lowers  $I$  at each  $V_G$  only by 1% or 2%. The contribution of  $\Delta\mu^0$  to  $G$  is negligible because the corresponding quantity

$$\Delta\hat{\mu}^0 = \left\{ \int_{y<0} - \int_{y>0} \right\} d^2\mathbf{r} f(\mathbf{r}) k_B T_K \ln [\lambda_D^2 n(\mathbf{r})], \quad (2.13)$$

is of the order of  $10^{-3}\Delta\mu^1$ . We also calculate  $G$  in the system with the reservoirs widened from the  $20 \times 20 \mu\text{m}^2$  squares to the  $20 \times 25 \mu\text{m}^2$  rectangles.  $G$  in the widened system is in the range of the error bar of  $G$  in the original system all over  $V_G$ . Moreover, we calculate  $G$  of the widened system with  $H = 20 \mu\text{m}$ , in which the obtained  $G$  in the widened system is in agreement with  $G$  in the original system.

# Chapter 3

## Results of the simulations

In this chapter, we present the obtained results from our simulations. The results clarify the origin of the steps [31], and give clues for understanding the electron dynamics behind the steplike conduction.

In Fig. 3.1(a), we plot  $G$  under the time average over 4,300,000 time steps and the ensemble average over 170 different initial conditions, where  $G$  exhibits weak steplike increases. Moreover,  $dG/dV_G$  in Fig. 3.1(b) shows a characteristic oscillation similar to that in Ref. [31].

The insulation for low  $V_G$  is due to the existence of a potential barrier in the gate; on the other hand, the increase in  $G$  for high  $V_G$  is for expansion of the width of a constriction in the gate. Figure 3.2 depicts the spatial distribution of the effective potential energy  $\Phi(\mathbf{r})$  near the gate [see Eq. (E.2)]. We should keep in mind that  $\Phi(\mathbf{r})$  is the sum of the confining potential and averaged electrostatic potential from self-organizing distributed electrons. As seen in Fig. 3.2(a), the existence of the high-energy barrier can be verified for low  $V_G$ . Figures 3.2(b)-(d) also display the decrease of the barrier height and the increase in the constriction width as  $V_G$  increases.

With the aid of  $\Phi(\mathbf{r})$ , we introduce the energy barrier defined by

$$E_B(V_G) \equiv \Phi(\mathbf{r}_G) - \int_{S_F} d^2\mathbf{r} f(\mathbf{r}; S_F) \Phi(\mathbf{r}), \quad (3.1)$$

which represents the potential energy difference between the center position in the gate,  $\mathbf{r}_G = (0, 0)$ , and the region in front of the gate,  $S_F = \{(x, y) | y_F \leq y \leq 0\}$ , with  $y_F = -1.7 \mu\text{m}$ . Here,  $y_F$  is selected so as to include an average position of the electron just in front of the gate, and

$$f(\mathbf{r}; S_F) = n(\mathbf{r}) / \bar{N}(S_F), \quad (3.2)$$

with  $\bar{N}(S_F) = \int_{S_F} d^2\mathbf{r} n(\mathbf{r})$  is the normalized single-particle distribution function in  $S_F$ . Figure 3.3 shows that  $E_B$  becomes zero at  $V_G = 0.15 \text{ V}$  ( $\equiv V_G(1)$ ) and the barrier exists for  $V_G < V_G(1)$ . However, a tiny current exists at  $V_G = 0.05 \text{ V}$  in Fig. 3.1(a), although the electrons cannot get over the barrier ( $E_B = 2.02 \text{ meV}$ ) because of the small kinetic energy  $k_B T_K = 0.103 \text{ meV}$  at  $T_K = 1.2 \text{ K}$ . The origin of the current will be discussed in Sec. 4.1.

The steplike behavior in  $G$  is roughly understood by examining the density distribution function  $n(\mathbf{r})$  [see Eq. (E.1)]. Figure 3.4 illustrates typical density patterns of electrons near the gate, corresponding to the  $s$ -th step of  $G$ . For low  $V_G$ , as seen in Fig. 3.4(a), the electrons seem to stay in front of the gate but flow slightly through the barrier. We can directly observe that the electrons flow through the gate in one line at the first step of  $G$  [Fig. 3.4(b)], two lines at the second step [Fig. 3.4(c)] and three lines at the third step [Fig. 3.4(d)]. Therefore, it is confirmed that the steplike increases are not originated from the conductance quantization [16], but the effects can be attributed to the increment in the number of stream lines of electron flow in the constriction, as suggested by Rees *et al.* [31]. However, the smooth steps

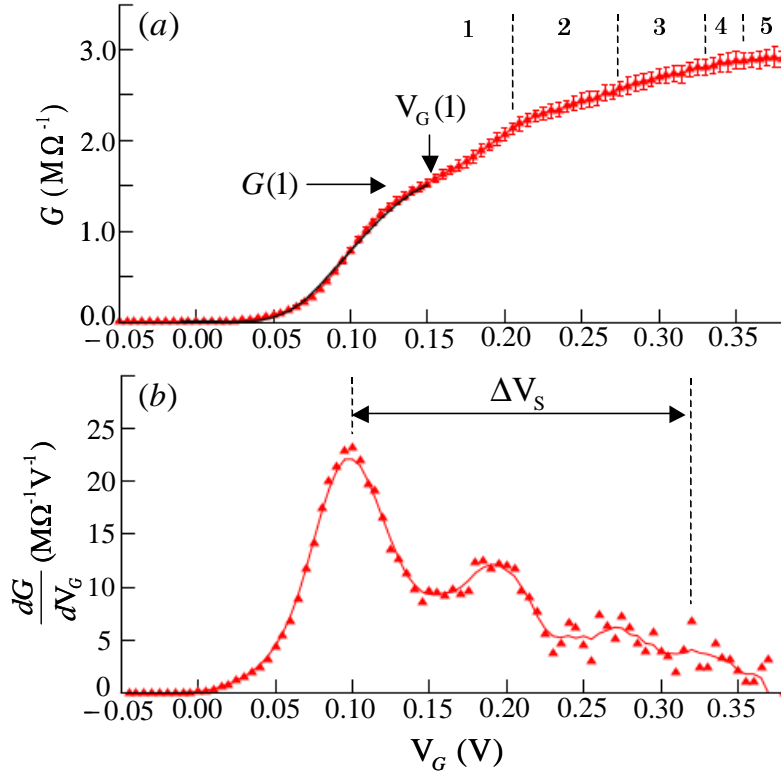


Figure 3.1: (a) The dc conductance  $G$  obtained from the MD simulations versus the gate voltage  $V_G$ , where each error bar represents the standard deviation of the ensemble average for each  $G$ , taken from [51]. Here,  $V_G(1) = 0.15$  V is the gate voltage at which the potential barrier  $E_B$  disappears, and  $G(1)$  is  $G$  at  $V_G(1)$ . The solid line is the approximate conductance  $\tilde{G}$  in Eq. (4.3). The vertical dashed lines and the number between them indicate the number of the stream lines organized by electrons in the gate, observed directly in the density distribution  $n(\mathbf{r})$ . (b)  $dG/dV_G$  with respect to  $V_G$  (red triangles) and the derivative of five-point unweighted smoothed  $G$  (red solid line), taken from [51]. Here, the range  $\Delta V_s = 0.202$  V between the vertical dashed lines runs from the first to the fourth peak in  $dG/dV_G$ .

in  $G$  cannot be understood only with the discrete increments in the number  $N_G$  of electrons to pass simultaneously through the gate.

As a possible mechanism for the smoothing, we can indicate the observed temporal variation of  $N_G$  in our simulations. To clarify this mechanism, we calculate the mean nearest-neighbor distance

$$\bar{r}_m(V_G) = \left\langle \theta \left[ \frac{3}{2} \bar{r} - r_{ij}(t) \right] r_{ij}(t) \middle| (S_{CL})_2^m \right\rangle, \quad (3.3)$$

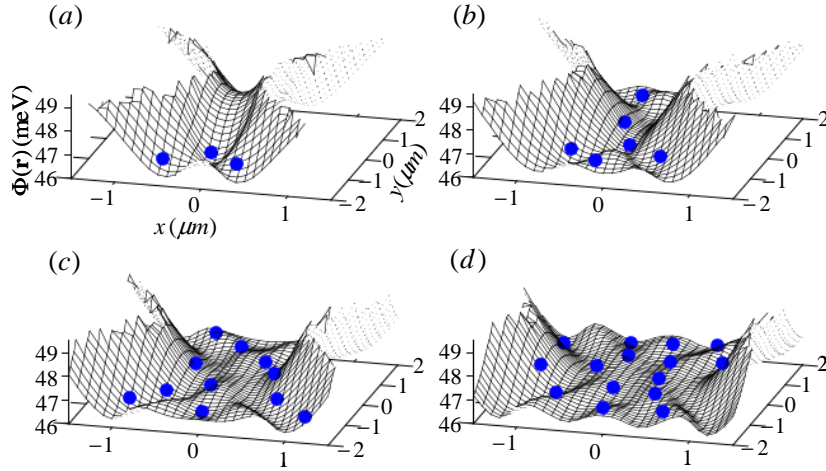


Figure 3.2: The spatial distribution of the potential energy  $\Phi(\mathbf{r})$  near the gate at  $V_G =$  (a) 0.09 V, (b)  $V_G = 0.18$  V, (c)  $V_G = 0.25$  V, and (d)  $V_G = 0.31$  V. Here, the blue spheres are placed at an electron configuration of a step in our simulations. These figures are taken from [51].

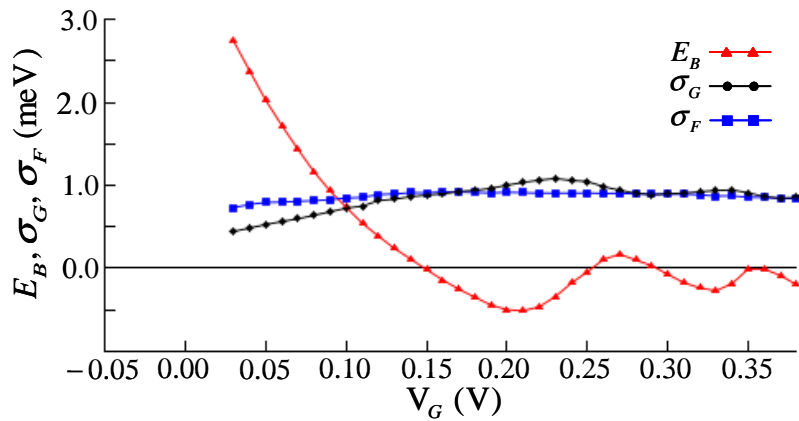


Figure 3.3: The potential barrier  $E_B$  in Eq. (3.1) (red triangles), and the standard deviations of temporally variational potential energy at the positions of the center of the gate,  $\sigma_G$  (black circles), and in front of the gate,  $\sigma_F$  (blue rectangles), taken from [51]. This figure is taken from [51].

among the electrons forming the  $m$ -electron current, which is the current when  $m$  electrons pass side by side through the constriction [see Eq. (E.5)]. Here, the region  $S_{\text{CL}} = \{(x, y) || y| \leq 0.05 \mu\text{m}\}$  is set in order to measure the separations in the confined direction. It is also to be noted that the average of  $r_{ij}$  in Eq. (3.3) is limited to the

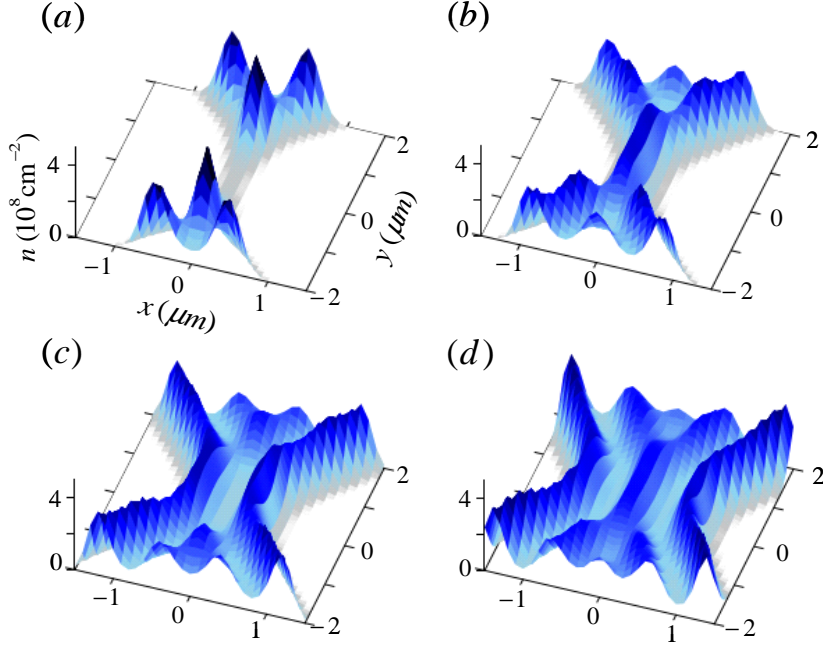


Figure 3.4: The density distribution  $n(\mathbf{r})$  near the gate at (a)  $V_G = 0.05$  V, (b)  $V_G = 0.15$  V, (c)  $V_G = 0.24$  V and (d)  $V_G = 0.30$  V. The lines observed in (b), (c), and (d) are formed by sequential single-electron flow. These figures are taken from [51].

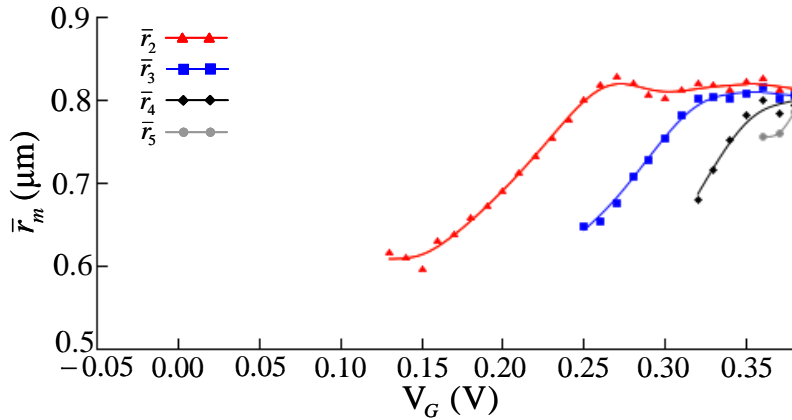


Figure 3.5: The mean nearest-neighbor distance  $\bar{r}_2$ ,  $\bar{r}_3$ ,  $\bar{r}_4$ , and  $\bar{r}_5$  in the  $x$  direction among the electrons organizing the two-, the three-, the four-, and the five-electron current, respectively. This figure is taken from [51].

middle distance of the nearest-neighbor and the second-neighbor distance. From  $\bar{r}_m$  for  $m = 2, 3, 4$ , and  $5$  plotted in Fig. 3.5, we find that the two-, three-, four-, and five-electron currents appear only in more than  $V_G = 0.13, 0.25, 0.32$ , and  $0.36$  V, respectively. These  $V_G$  are lower than the  $V_G$  at which the  $m$  lines are observed in  $n(\mathbf{r})$  [see Fig 3.1(a)]. In addition, we find intermediate states in which the  $m$ -electron current with long separations and the  $(m + 1)$ -electron current with short separations coexist. Since  $G$  in the intermediate states takes between  $m$ - and  $(m + 1)$ -electron current conductance, the effect can lead to the gradual change in  $G$ . These results also reveal that the separations between electrons to pass side by side through the gate have a fluctuation margin about  $0.1 \mu\text{m}$  from the average inter-electron separation  $\bar{r} \approx 0.77 \mu\text{m}$ . A major factor in the temporally fluctuational separations will be specified in Sec. 4.1.



# Chapter 4

## Discussion

In this chapter, we first discuss the origin of the current under the existence of the potential barrier and the mechanism smoothing the steps in the conductance. Next, we compare the conductance in our system with the observed conductance in the device [31]. Finally, the obtained conductance from the LD simulations is briefly compared with that from the MD simulations.

### 4.1 Density-fluctuation-affected transport properties

In this section, we propose two mechanisms of smoothing the steps in  $G$ . We attribute the current for  $V_G < V_G(1)$  to the intermittent disappearances of the barrier due to temporal fluctuation of the potential at both  $\mathbf{r}_G$  and  $S_F$ . This mainly results from the following two reasons. First, the standard deviation of temporally variational potential energy in the channel

$$\bar{\sigma} = \int_{|y| < D} d^2\mathbf{r} f(\mathbf{r}; |y| < D) \sigma(\mathbf{r}) \approx 0.7 \text{meV}, \quad (4.1)$$

with Eq. (E.3), is much larger than  $k_B T_K$ . Second, the velocity distribution in the  $y$  direction near the gate for  $V_G < V_G(1)$  has the nearly zero mean value ( $\sim 10^{-4} - 10^{-7}$  meV in terms of the kinetic energy), and thus does not deviate from the equilibrium distribution. Therefore, the conductor-insulator transition in our system is not caused by pinning and depinning of electrons at the constriction [25].

From the conservation of energy, it is clear that electrons can pass through the gate only when the potential energy exceeds the barrier. Therefore,  $G$  up to  $V_G(1)$  may be approximately represented as  $G \approx \tilde{G} = G(1)P(1)$ , where  $G(1)$  is the conductance at  $V_G(1)$  and  $P(1)$  is the probability that the potential energy of the front electron exceeds the potential energy at  $\mathbf{r}_G$ . From the direct calculations in terms of the MD (see Appendix F), we verify that the temporal change of  $\phi(\mathbf{r}, t)$  almost satisfies the

normal distributions as follows:

$$\langle \delta [\epsilon - \phi(\mathbf{r}, t)] | (\delta \mathbf{r})_1 \rangle \approx \frac{\exp \left\{ -\frac{[\epsilon - \Phi(\mathbf{r})]^2}{2\sigma(\mathbf{r})^2} \right\}}{\sqrt{2\pi\sigma(\mathbf{r})^2}}, \quad (4.2)$$

as in the case of the fluctuating electric field [64]. Furthermore, it is probable that the temporal changes of  $\phi(\mathbf{r}, t)$  are uncorrelated between the two points of space. This is because the potential of the electron just in front of the barrier is fluctuated mostly by two electrons in the rear [see Figs. 3.2(a) and 3.4(a)]; on the other hand, the potential at  $\mathbf{r}_G$  is fluctuated mostly by the electron of the other side across the barrier. Hence,  $\tilde{G}$  can be estimated as

$$\begin{aligned} \tilde{G} &\approx \frac{G(1)}{C} \int_{-\infty}^{\infty} d\epsilon \int_{\epsilon}^{\infty} d\epsilon' \frac{\exp \left[ -\frac{\epsilon'^2}{2\sigma_F^2} \right]}{\sqrt{2\pi\sigma_F^2}} \frac{\exp \left[ -\frac{(\epsilon - E_B)^2}{2\sigma_G^2} \right]}{\sqrt{2\pi\sigma_G^2}} \\ &= G(1) \operatorname{erfc} \left[ \frac{E_B}{\sqrt{2(\sigma_F^2 + \sigma_G^2)}} \right], \end{aligned} \quad (4.3)$$

where

$$C = \operatorname{erfc} \left[ \frac{E_B}{\sqrt{2(\sigma_F^2 + \sigma_G^2)}} \right] \Big|_{E_B=0},$$

is the probability for  $E_B = 0$ ;  $\sigma_G(V_G) = \sigma(\mathbf{r}_G)$  and  $\sigma_F(V_G) = \int_{S_F} d^2\mathbf{r} f(\mathbf{r}; S_F) \sigma(\mathbf{r})$  are, respectively, the standard deviation of the potential energy at  $\mathbf{r}_G$  and in  $S_F$  (see Fig. 3.3); and  $\operatorname{erfc}[x]$  is the complementary error function [solid line of Fig. 3.1(a)]. Although  $\tilde{G}$  is estimated on the basis of only the one necessary condition, nevertheless  $\tilde{G}$  is in good agreement with  $G$  calculated in our simulations.

It should also be noted that the rising of  $G$  takes place at  $V_G$  at which  $E_B$ ,  $\sigma_F$ , and  $\sigma_G$  satisfy the relation

$$E_B \simeq 2\sigma_F + 2\sigma_G, \quad (4.4)$$

where tails of the potential distribution at the two different points touch just each other. Therefore, this may give a method of an approximate estimation of the potential fluctuation from the potential energy.

Concerning the choice of  $y_F$  in  $S_F$  [see Eq. (3.1)], the discussion on  $\tilde{G}$  holds well for the range of  $-2.3 \mu\text{m} \leq y_F \leq -1.3 \mu\text{m}$  in which the deviation  $|\tilde{G} - G|$  at each  $V_G$  is less than  $0.04 \text{ M}\Omega^{-1}$ . Outside the range,  $\tilde{G}$  becomes discrepant from  $G$  because of large spatial variation in  $\sigma(\mathbf{r})$ . Figure 4.1 illustrates that  $\sigma(\mathbf{r})$  increases in incommensurate regions in which two structures with the different number of the lines in  $n(\mathbf{r})$  are frustrated [23, 24, 67, 68].

As seen in Sec. 3, the temporal variation of  $N_G$  arises from the fluctuational inter-electron separations in the confined direction. The variational separations can be

understood from an effect of the density fluctuation. The root-mean-square displacement  $\delta_x$  in the  $x$  direction estimated from the harmonic approximation by equalizing  $\delta_x^2 \nabla^2 \phi_1(\bar{r})$  to  $k_B T_K/2$  [64, 69], i.e.,

$$\delta_x = \sqrt{\frac{k_B T_K}{2 \nabla^2 \phi_1(\bar{r})}}. \quad (4.5)$$

is given by  $\delta_x = 0.119 \mu\text{m}$ , which is comparable with the fluctuation margin. The observed crystal-like ordering in the confined direction in the density patterns in Fig. 3.4 also supports of our estimation. Therefore, we attribute grounds for the temporal change of  $N_G$  to the short wave-length density fluctuation.

In the above discussion, we suppose that the smooth rising from the insulating state to the first step in  $G$  is due to the potential fluctuation, and the smooth steps in  $G$  are caused by the vibration in the confined direction. These dynamics can be commonly attributed by the density fluctuations. Therefore, the magnitude of the density fluctuation seems to determine whether the steps in  $G$  can be observed.

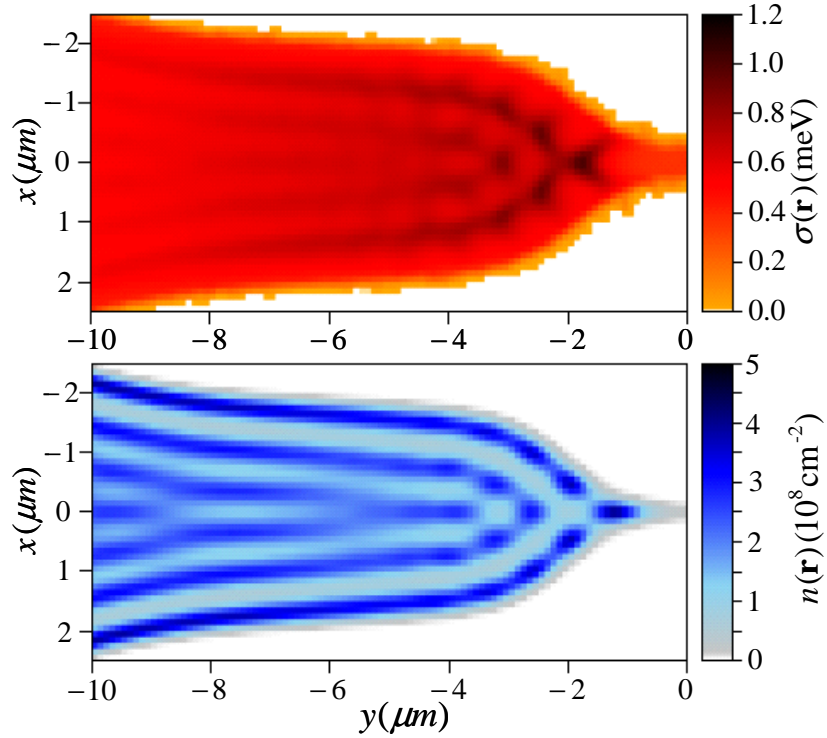


Figure 4.1: The spatial distribution of potential fluctuation  $\sigma(\mathbf{r})$  (upper figure), and the density distribution  $n(\mathbf{r})$  (lower figure) at  $V_G = 0.05 \text{ V}$  in the region of  $-10 \mu\text{m} \leq y \leq 0 \mu\text{m}$ . These figures are taken from [51].

## 4.2 Comparison of our result with the observed conductance

In this section, we illustrate the qualitative consistency between our and experiment conductance in order to stress the suitability of our approach for the electron system in the device [31].

The scaled and shifted  $G$  are similar to the measured conductance  $G_E$  in Ref. [31] as seen in Fig. 4.2. First, we select a scale factor  $g = 1.414$  so that the magnitude of  $G$  at the first step fits into that of  $G_E$ . For our system, the magnitude of  $G$  is dependent on the insertion areas  $A_L$  and  $A_R$ . This is caused by the change of space distribution of the chemical potential in the reservoirs (see Fig. D.2 in Appendix D).

Second, we select a constant  $\Delta V_E/\Delta V_S = 3.3$  as a scale factor for  $G$  in the  $V_G$  direction, where  $\Delta V_S$  and  $\Delta V_E$  are the amount of increase in  $V_G$  with an increment of  $N_G$  from 1 to 4 in the simulation and the experiment [31], respectively [see Figs. 3.1(b) and 4.2(b)]. The choice of the scale factor stands on the consensus that a steplike increase in conductance is determined by  $N_G$ . Because  $\Delta V_E$  decreases with decreasing electron density, as observed in Ref. [31], and the density  $\bar{n} \approx 2.2 \times 10^8 \text{ cm}^{-2}$  in the simulations is lower than the experimental density  $\bar{n}_E = 1.5 \times 10^9 \text{ cm}^{-2}$  [31], the result of  $\Delta V_S < \Delta V_E$  is reasonable.

Third, we shift  $G$  so that  $V_G(1)$  agrees with the first-minimum-gate voltage  $V_G^E(1)$  which corresponds to the minimum between the first and the second peak in  $dG_E/dV_G$  [see Fig. 4.2(b)]. Because the guard voltage 0.62 V in the device corresponds to 0 V in our system,  $V_G(1)$  is practically larger than  $V_G^E(1)$  by  $\{V_G^E(1) - 0.62\} - \{V_G(1) - 0\} = 0.135$  V. The shift is also valid. Indeed, the shift of conductance into the lower  $V_G$  direction with increasing electron density is observed both in the experiment [31] and our system (see Fig. D.3 in Appendix D).

As a result of the above discussion,  $G$  transformed into  $G_T$  in Fig. 4.2(a) is almost in agreement with  $G_E$  for  $V_G > V_G^E(1)$ , but is not good for  $V_G < V_G^E(1)$ . The disagreement for  $V_G < V_G^E(1)$  is also reasonable, for the amount of increase in  $V_G$  with the growth in conductance from the threshold of current flow to the first step is almost invariant with respect to electron density [31] (see Fig. D.3 in Appendix D). For  $V_G < V_G(1)$ , the shifted  $G$  without scaling of  $\Delta V_E/\Delta V_S$  is actually coincident with  $G_E$  for  $V_G < V_G^E(1)$  as seen in Fig. 4.2 (c).

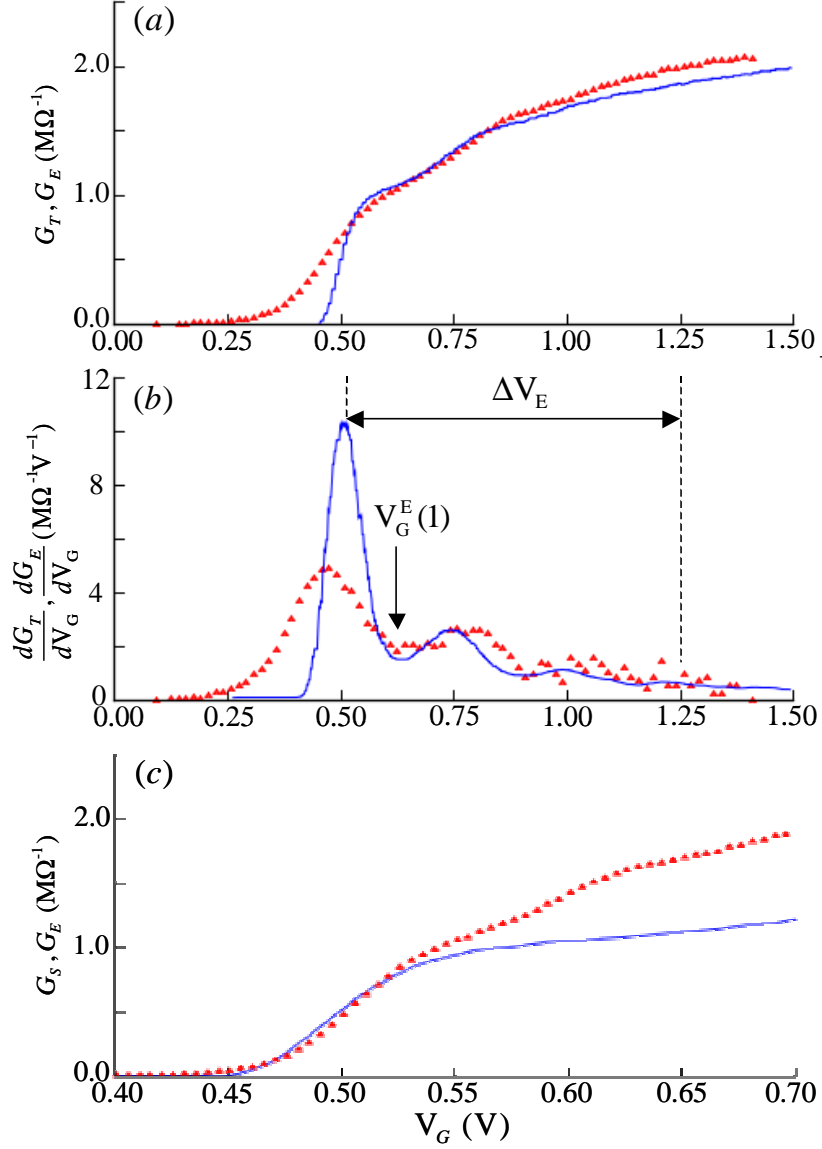


Figure 4.2: (a) The measured conductance  $G_E$  in the experiment (blue solid line) [31] and  $G(V_G)$  in Fig. 3.1(a) transformed into  $G_T(V_G) = G\{[V_G + V_G(1)]\Delta V_S/\Delta V_E - V_G^E(1)\}/g$  (red triangles) vs the gate voltage  $V_G$ , taken from [51]. Here,  $V_G(1)$  and  $\Delta V_S$  are given in Fig. 3.1, and  $\Delta V_E$  and  $V_G^E(1)$  are shown below. (b)  $dG_E/dV_G$  (blue solid line) [31] and  $dG_T/dV_G$  (red solid triangles), with respect to  $V_G$ , taken from [51]. Here, the range  $\Delta V_E = 0.750$  V between the vertical dashed lines runs from the first to the fourth peak in  $dG_E/dV_G$ .  $V_G^E(1) = 0.63$  V indicates  $V_G$ , corresponding to the experimental counterpart of  $V_G(1)$  in the simulations. (c)  $G_E$  (blue solid line) and  $G(V_G)$  in Fig. 3.1(a) transformed into  $G_S(V_G) = G(V_G + \Delta V_G)/g$  (red triangles) vs the gate voltage  $V_G$ , where  $\Delta V_G = 0.4063$  V is a fitting parameter.

### 4.3 Langevin dynamics simulation

We also calculate the conductance in the molecular dynamics under the Langevin thermostat, which is known as the Langevin dynamics, to check how the results depend on our choice of the Nosé-Hoover thermostat.

Firstly, we explain the method of LD simulation to calculate the conductance of electrons [89]. The equation of motion for the electrons in the LD simulations is given by

$$m \frac{d^2 r_i^\alpha}{dt^2} = F_i^\alpha - m \xi \dot{r}_i^\alpha + \tilde{F}_i^\alpha, \quad (4.6)$$

associated with Eqs. (2.9) and (2.10), where  $F_i^\alpha$  consists of the first, third, and fourth terms of the right-hand side in Eq. (2.7),  $\xi$  is the friction constant, and  $\tilde{F}_i^\alpha$  is a random force, reproducing the thermal noise with zero mean value and variance  $\langle \tilde{F}_i^\alpha(t) \tilde{F}_j^\beta(t') \rangle = 2mk_B T \xi \delta_{ij} \delta_{\alpha\beta} \delta(t-t')$ . If we regard  $\xi$  as the collision frequency through the Einstein' relation, we may estimate  $\xi$  as  $\xi \simeq \nu^{se}$  (see Appendix B.1 for  $\nu^{se}$ ). For the value to be  $\xi \ll \nu_{ee}$ , we have no reason to neglect the inertial term, where  $\nu_{ee}$  is the electron-electron collision frequency (see Appendix B.1). To integrate Eq. (4.6), we adopt the Ermak's approach [89,90], which performs properly the stochastic integration [91]. This LD simulation is reduced to an overdamped LD simulation for  $t_0 \xi \gg 1$ , and our MD simulation without the Nosé-Hoover thermostat in the limit  $\xi \rightarrow 0$ . The other numerical methods and the simulation setup are unchanged from those of the MD simulations (see Sec. 2).

Figure 4.3 is the corresponding plot to Fig. 3.1(a) for the LD simulations. The obtained  $G_L$  in Fig. 4.3 under the averages of 4,300,000 time steps and 16 different initial conditions reproduces the steplike conductance as observed in Ref. [31], and shows qualitatively similar behavior to  $G$  in Fig. 3.1(a). However, we can find the sharper rising to the first step of  $G_L$  than that of  $G$ . This deference reflects on the observed smaller potential fluctuation in the LD simulations than that in the MD simulations (see Sec. 4.1). Because the characteristic time scale of the relaxation of electron motion is  $1/\xi$ , which is introduced in Eq. (C1) [71], the reduction in potential fluctuation may result from the damping. A more detailed comparison between MD and LD will be discussed in future work.

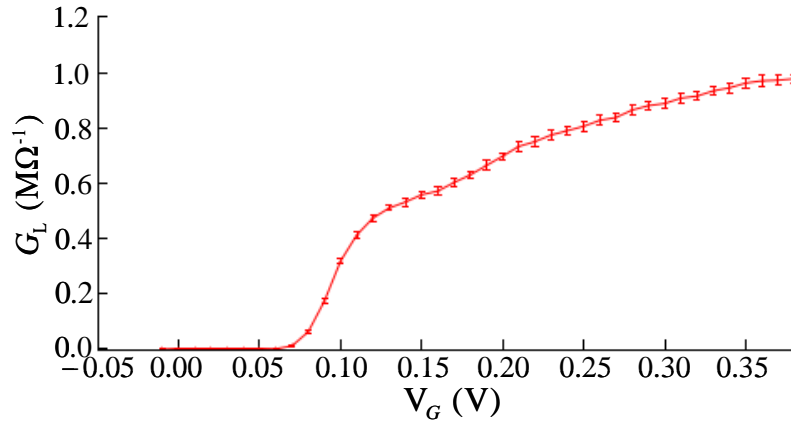


Figure 4.3: (a) The dc conductance  $G_L$  obtained from the LD simulations versus the gate voltage  $V_G$ , where each error bar represents the standard deviation of the ensemble average for each  $G_L$ , taken from [51].



# Chapter 5

## Conclusion

In conclusion, we reproduce the steplike conductance in a classical 2D electron system confined in the point-contact device on liquid  $^4\text{He}$  by the molecular dynamics simulation. Conductance in two-dimensional electrons confined in the shape of a microchannel with a point contact by electric fields is calculated as a function of the confinement strength of the contact. It is confirmed that the number of the steps corresponds to the number of stream lines formed by the flow of self-organizing distributed electrons at the contact. This result supports the expectation by Rees *et al.* [31] in which the conductance does not originate from quantum effects but from classical many-particle effects at the contact. We verify that a potential barrier exists in the contact for the stronger confinement than that at the first step, and disappears for the weaker confinement in which the constriction width of the contact increases with weakening confinement. In the strong confinement, the rising of the conductance can be attributed to intermittent disappearances of the barrier due to temporal fluctuation of the electrostatic potential. In the weak confinement, the number of electrons to pass simultaneously through the contact varies temporally, which plays a certain role in smoothing the step in conductance. This change may result from the short wave-length density fluctuation in the confined direction at the contact. Therefore, we suppose that the discontinuous properties by the strong correlation effects are enhanced in confined geometry, which affects the transport.

As a final remark, we briefly comment on a recent paper on the same subject based on both the experiment and MD [70]. Although our work differs in temperature range from the paper, which makes a study of the transport of the Wigner crystal [70], the electron dynamics clarified by our investigations also provides information to help them understand the mechanism.



# Appendix A

## Electric potential, quantized electron states, and classical 2D Hamiltonian

In this appendix, we first derive electric potential for electrons over liquid  ${}^4\text{He}$  on metal electrodes, and evaluate the contribution of screening effects in the potential due to the existence of liquid  ${}^4\text{He}$ . Next, we introduce Hamiltonian for the electrons from the electric potential based on the numerical evaluations, investigate electron states in the vertical direction against the liquid surface, and derive effective 2D Hamiltonian for motion on the liquid surface. Finally, we discuss the difference of electric potential between our system and the device structure in the experiment [31].

### A.1 Derivation of electric potential

In this subsection, we derive electric potential for electrons over liquid  ${}^4\text{He}$  on metal electrodes. First of all, we consider an electron system in the 3D space occupied by metal electrodes for  $0 \geq z$  and filled with liquid  ${}^4\text{He}$  with the dielectric constant  $\epsilon_h \approx 1.057$  for  $z_h > z > 0$  (see Fig. A.1). The electrons are artificially added over liquid  ${}^4\text{He}$  [28, 31] and do not penetrate liquid  ${}^4\text{He}$  due to the exclusion effect of the helium atoms [72, 73], and thus are distributed for  $z > z_h$ .

For this system, the electric potential at the position  $\mathbf{R}$  at time  $t$  is determined by the Poisson equation

$$\epsilon(z)\nabla^2\phi^{\text{EP}}(\mathbf{R}, t) = -4\pi\rho(\mathbf{R}, t), \quad (\text{A.1})$$

under boundary conditions, with the electron density

$$\rho(\mathbf{R}, t) = -e \sum_{i=1}^N \delta[\mathbf{R} - \mathbf{R}_i(t)], \quad (\text{A.2})$$

where  $\epsilon(z) = \epsilon_h$  for  $z_h > z > 0$  and  $\epsilon(z) = 1$  for  $z > z_h$ ,  $\mathbf{R}_i(t)$  is the position of the  $i$ -th electron at time  $t$ ,  $e$  is the elementary electric charge, and  $N$  is the particle

number of electrons. At the interface of the liquid  ${}^4\text{He}$  at  $z = z_h$ ,  $\phi^{\text{EP}}$  must satisfy the boundary condition

$$\begin{aligned}\phi^{\text{EP}}[\mathbf{r}, z(> z_h) \rightarrow z_h] &= \phi^{\text{EP}}[\mathbf{r}, z(< z_h) \rightarrow z_h] \\ \frac{\partial \phi^{\text{EP}}[\mathbf{r}, z(> z_h) \rightarrow z_h]}{\partial z} &= \epsilon_h \frac{\partial \phi^{\text{EP}}[\mathbf{r}, z(< z_h) \rightarrow z_h]}{\partial z}.\end{aligned}\quad (\text{A.3})$$

We also impose the electric voltages  $V_S$  and 0 upon a region  $S$  and the outside of  $S$  on the electrode surface at  $z = 0$ , i.e., the boundary conditions at  $z = 0$  are <sup>1</sup>

$$\phi^{\text{EP}}(\mathbf{r}, z = 0) = \begin{cases} V_S & (\mathbf{r} \in S) \\ 0 & (\mathbf{r} \notin S). \end{cases}\quad (\text{A.4})$$

From these boundary conditions and the natural supposition of a field satisfying  $\phi^{\text{EP}}(\mathbf{r}, z) = 0$  for  $|\mathbf{r}|$  or  $z \rightarrow \infty$ , the solution of Eq. (A.1) is given by [52, 53]

$$\phi^{\text{EP}}(\mathbf{R}, t) = 4\pi \int_{z \geq 0} dV_0 \rho(\mathbf{R}_0) \mathcal{G}(\mathbf{R}, \mathbf{R}_0) - V_S \int_S d\mathbf{S}_0 \cdot \nabla_0 \mathcal{G}(\mathbf{R}, \mathbf{R}_0) |_{z_0=0}.\quad (\text{A.5})$$

Here,  $\mathcal{G}$  is the Green function which satisfies the equation

$$\epsilon(z) \nabla^2 \mathcal{G}(\mathbf{R}, \mathbf{R}_0) = -\delta(\mathbf{R} - \mathbf{R}_0).\quad (\text{A.6})$$

This equation is subject to the boundary conditions:

$$\begin{aligned}\mathcal{G}[\mathbf{r}, z(> z_h) \rightarrow z_h; \mathbf{R}_0] &= \mathcal{G}[\mathbf{r}, z(< z_h) \rightarrow z_h; \mathbf{R}_0] \\ \frac{\partial \mathcal{G}[\mathbf{r}, z(> z_h) \rightarrow z_h; \mathbf{R}_0]}{\partial z} &= \epsilon_h \frac{\partial \mathcal{G}[\mathbf{r}, z(< z_h) \rightarrow z_h; \mathbf{R}_0]}{\partial z},\end{aligned}\quad (\text{A.7})$$

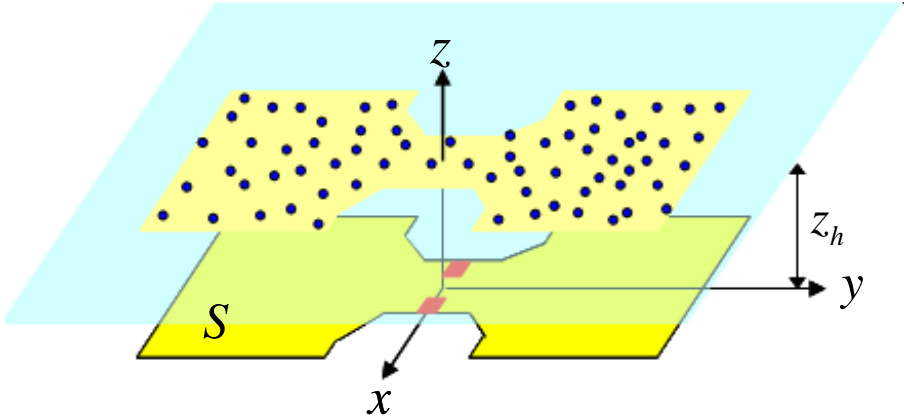


Figure A.1: A schematic view of our system with the screening effect due to the existence of liquid  ${}^4\text{He}$ . In the system, the 3D space is occupied with metal electrodes  $0 \geq z$  and filled with liquid  ${}^4\text{He}$   $z_h > z > 0$ , in which electrons are distributed in  $z > z_h$  (blue circles). On the conductor surface at  $z = 0$ , the electric voltages  $V_S$  and the 0 are imposed upon the colored regions  $S$  and the outside of  $S$ , respectively.

<sup>1</sup>Here, we consider the case of  $S = S_0 \cup S_G$  and  $V_S = V_0 = V_G$  for the boundary conditions in Eq. (2.4)

and

$$\mathcal{G}(\mathbf{r}, z; \mathbf{r}_0, z_0) = \begin{cases} 0 & (z \text{ or } z_0 = 0) \\ 0 & (z \text{ or } z_0 \rightarrow \infty) \\ 0 & (|\mathbf{r}| \text{ or } |\mathbf{r}_0| \rightarrow \infty). \end{cases} \quad (\text{A.8})$$

The Green function  $\mathcal{G}(\mathbf{R}; \mathbf{R}_0)$  for  $z > z_h$  is explicitly given by [74]

$$\begin{aligned} \mathcal{G}(\mathbf{R}; \mathbf{R}_0) = & \frac{1}{4\pi} \left[ \frac{1}{\sqrt{|\mathbf{r} - \mathbf{r}_0|^2 + (z - z_0)^2}} - \frac{1}{\sqrt{|\mathbf{r} - \mathbf{r}_0|^2 + (z + z_0)^2}} \right. \\ & \left. + \sum_{n=1}^{\infty} \left\{ \frac{(-\sigma)^n}{\sqrt{|\mathbf{r} - \mathbf{r}_0|^2 + \{z + z_0 + 2z_h(n-2)\}^2}} - \frac{(-\sigma)^n}{\sqrt{|\mathbf{r} - \mathbf{r}_0|^2 + \{z + z_0 + 2z_h n\}^2}} \right\} \right], \end{aligned} \quad (\text{A.9})$$

with

$$\sigma = \frac{\epsilon_h - 1}{\epsilon_h + 1}. \quad (\text{A.10})$$

In the bracket  $[\dots]$  of the right-hand side of Eq. (A.9), the first term is the bare Coulomb potential at  $\mathbf{R}$  when a unit charge is placed at  $\mathbf{R}_0$ , and the second and the third terms are, respectively, the contribution of the induced charge in the metal electrode and the liquid  $^4\text{He}$ . The contribution works as the screening effects for the bared Coulomb potential. It should also be noted that Eq. (A.10) satisfies the charge neutrality condition at each degree of  $\sigma$ . From Eqs. (A.5) and (A.9),  $\phi^{\text{EP}}(\mathbf{R}, t)$  for  $z > z_h$  can be represented as

$$\phi^{\text{EP}}(\mathbf{R}, t) = \phi_{\text{I}}^{\text{EP}}(\mathbf{R}, t) + \phi_{\text{C}}^{\text{EP}}(\mathbf{R}) \quad (\text{A.11})$$

with

$$\begin{aligned} \phi_{\text{I}}^{\text{EP}}(\mathbf{R}, t) = & -e \sum_{i=1}^N \left[ \frac{1}{\sqrt{|\mathbf{r} - \mathbf{r}_i|^2 + (z - z_i)^2}} - \frac{1}{\sqrt{|\mathbf{r} - \mathbf{r}_i|^2 + (z + z_i)^2}} \right. \\ & \left. + \sum_{n=1}^{\infty} \left\{ \frac{(-\sigma)^n}{\sqrt{|\mathbf{r} - \mathbf{r}_i|^2 + \{z + z_i + 2z_h(n-2)\}^2}} - \frac{(-\sigma)^n}{\sqrt{|\mathbf{r} - \mathbf{r}_i|^2 + \{z + z_i + 2z_h n\}^2}} \right\} \right] \end{aligned} \quad (\text{A.12})$$

and

$$\begin{aligned} \phi_{\text{C}}^{\text{EP}}(\mathbf{R}) = & \frac{V_S}{4\pi} \int_S dx_0 dy_0 \left[ \frac{2z}{[|\mathbf{r} - \mathbf{r}_0|^2 + z^2]^{3/2}} \right. \\ & \left. - \sum_{n=1}^{\infty} \left\{ \frac{(-\sigma)^n \{z + 2z_h(n-2)\}}{[|\mathbf{r} - \mathbf{r}_0|^2 + \{z + 2z_h(n-2)\}^2]^{3/2}} - \frac{(-\sigma)^n \{z + 2z_h n\}}{[|\mathbf{r} - \mathbf{r}_0|^2 + \{z + 2z_h n\}^2]^{3/2}} \right\} \right] \end{aligned} \quad (\text{A.13})$$

## A.2 Evaluation of the screening effect due to the existence of liquid ${}^4\text{He}$

In this subsection, we evaluate the magnitude of the the screening effect due to the existence of liquid  ${}^4\text{He}$ , and show the smallness of the effect. In Eq. (A.9), the terms including to  $\sigma$  become smaller as the exponent of  $\sigma$  increases because of  $\sigma \approx 0.028$ . In order to evaluate the contribution of the terms, we divide  $\mathcal{G}(\mathbf{R}; \mathbf{R}_0)$  into the four terms: the zeroth-degree term of  $\sigma$  is given by

$$\mathcal{G}_0(r, z_h) = \frac{1}{4\pi} \left[ \frac{1}{r} - \frac{1}{\sqrt{r^2 + 4z_h^2}} \right], \quad (\text{A.14})$$

the first-degree term of  $\sigma$  is

$$\mathcal{G}_1(r, z_h) = -\frac{\sigma}{4\pi} \left[ \frac{1}{r} - \frac{1}{\sqrt{r^2 + 16z_h^2}} \right], \quad (\text{A.15})$$

the second-degree term of  $\sigma$  is

$$\mathcal{G}_2(r, z_h) = \frac{\sigma^2}{4\pi} \left[ \frac{1}{\sqrt{r^2 + 4z_h^2}} - \frac{1}{\sqrt{r^2 + 36z_h^2}} \right], \quad (\text{A.16})$$

and the all terms over the second-degree term of  $\sigma$  are summarized as

$$\mathcal{G}_{\geq 3}(r, z_h) = \frac{1}{4\pi} \sum_{n=3}^{\infty} \left[ \frac{(-\sigma)^n}{\sqrt{r^2 + \{2z_h(n-1)\}^2}} - \frac{(-\sigma)^n}{\sqrt{r^2 + \{2z_h(n+1)\}^2}} \right]. \quad (\text{A.17})$$

Here, we presume that all electrons place at  $z = z_h$ , whose validity will be demonstrated in Sec. A.3. The ratio of  $\mathcal{G}_1(r, z_h)$  to  $\mathcal{G}_0(r, z_h)$ , and  $\mathcal{G}_2(r, z_h)$  to  $\mathcal{G}_0(r, z_h)$  are, respectively, given by

$$\frac{|\mathcal{G}_1(r, z_h)|}{\mathcal{G}_0(r, z_h)} < \frac{|\mathcal{G}_1(r \rightarrow \infty, z_h)|}{\mathcal{G}_0(r \rightarrow \infty, z_h)} \simeq 4\sigma \approx 0.11, \quad (\text{A.18})$$

and

$$\frac{\mathcal{G}_2(r, z_h)}{\mathcal{G}_0(r, z_h)} < \frac{\mathcal{G}_2(r \rightarrow \infty, z_h)}{\mathcal{G}_0(r \rightarrow \infty, z_h)} \simeq 10\sigma^2 \approx 0.0078. \quad (\text{A.19})$$

We can also evaluate the upper limit of  $\mathcal{G}_{\geq 3}(r, z_h)$  as follows:

$$|\mathcal{G}_{\geq 3}(r, z_h)| < \left| \frac{\sigma^3}{4\pi z_h} \frac{3-2\sigma}{12} \right| \approx \frac{4.3 \times 10^{-7}}{z_h} [\mu\text{m}^{-1}]. \quad (\text{A.20})$$

This contribution is significantly smaller than  $\mathcal{G}_0(r, z_h)$  for the inter-electron separations in the system we treat,  $r \sim 0.1z_h$ .

### A.3 Quantized electron states in the vertical direction against the liquid surface and effective 2D Hamiltonian

In this subsection, we constitute Hamiltonian for the electrons from the electric potential obtained in Sec. A.1 based on the numerical evaluations in Sec. A.2. We also investigate electron states in the vertical direction against the liquid surface, and derive an effective 2D Hamiltonian for motion along the liquid surface.

The Hamiltonian for the electrons interacting through  $\phi^{\text{EP}}$  under the first-order approximation of  $\sigma$  is given by

$$\begin{aligned}
 H \simeq & -\frac{\hbar^2}{2m} \sum_{i=1}^N \frac{\partial^2}{\partial \mathbf{R}_i^2} + \sum_{i>j} \frac{e^2}{\sqrt{r_{ij}^2 + (z_i - z_j)^2}} + E_{\text{He}} \theta(z_h - z_i) \\
 & - \frac{1}{2} \sum_{i,j} \left[ \frac{e^2}{\sqrt{r_{ij}^2 + (z_i + z_j)^2}} + \frac{\sigma e^2}{\sqrt{r_{ij}^2 + (z_i + z_j - 2z_h)^2}} - \frac{\sigma e^2}{\sqrt{r_{ij}^2 + (z_i + z_j + 2z_h)^2}} \right] \\
 & - \frac{eV_S}{4\pi} \sum_{i=0}^N \int_S d^2r_0 \left[ \frac{2z_i}{[r_{i0}^2 + z_i^2]^{3/2}} - \frac{\sigma \{z_i - 2z_h\}}{[r_{i0}^2 + \{z_i - 2z_h\}^2]^{3/2}} + \frac{\sigma \{z_i + 2z_h\}}{[r_{i0}^2 + \{z_i + 2z_h\}^2]^{3/2}} \right],
 \end{aligned} \tag{A.21}$$

where the term  $E_{\text{He}} \theta(z_h - z_i)$  is the effective representation of the exclusion effect of the helium atoms [72], and the prefactor 1/2 of the interaction between the electrons

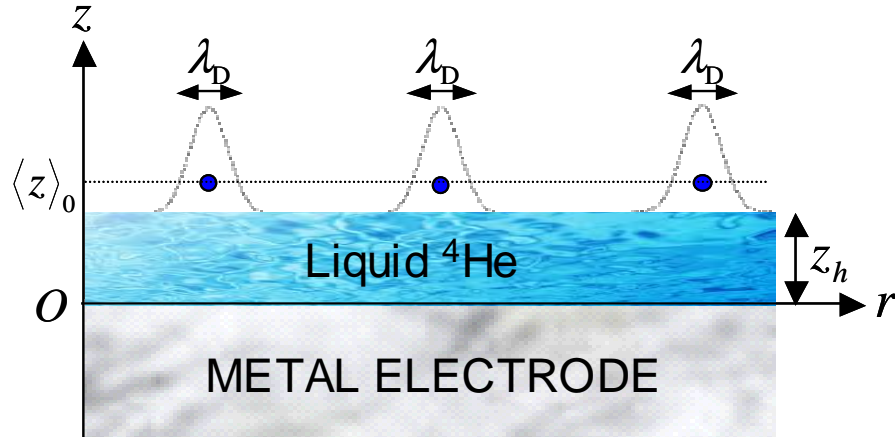


Figure A.2: A schematic view of the electron states for the electrons over liquid  ${}^4\text{He}$  on metal electrodes. All electrons are placed at the average position in the quantum ground state,  $\langle z \rangle_0$ . The corn-shaped dotted lines represent the schematic electron wavefunction in the direction parallel to the liquid surface.

and the induced charges comes from the self energy of the induced charges [75] [the step function  $\theta$  is introduced in Eq. (2.7)]. We also suppose  $z_i = z_j$  ( $i \neq j$ ) and  $|z_i - z_h| \ll r_{ij}$ ,  $z_i$ ,  $z_h$ , and apply the first-order approximation of  $\sigma$  and  $|z_i - z_h|$  to  $H$ . Consequently,  $H$  reduces to

$$\begin{aligned}
H &= -\frac{\hbar^2}{2m} \sum_{i=1}^N \frac{\partial^2}{\partial \mathbf{r}_i^2} + \sum_{i>j} \left[ \frac{e^2}{r_{ij}} - \frac{e^2}{\sqrt{r_{ij}^2 + 4z_h^2}} + \frac{8e^2\sigma z_h^2}{r_{ij}^3} \right] \\
&- \frac{eV_S}{4\pi} \sum_{i=0}^N \int_S d^2r_0 \left[ \frac{(2+\sigma)z_h}{[r_{i0}^2 + z_h^2]^{3/2}} + \frac{3\sigma z_h}{[r_{i0}^2 + 9z_h^2]^{3/2}} \right] \\
&+ \sum_{i=1}^N \left[ -\frac{\hbar^2}{2m} \frac{\partial^2}{\partial z_i^2} - \frac{\sigma e^2}{4(z_i - z_h)} + \left\{ \frac{e^2}{4z_h^2} + eF_{\perp}(\mathbf{r}_i) \right\} (z_i - z_h) + E_{\text{He}}\theta(z_h - z_i) \right],
\end{aligned} \tag{A.22}$$

with the holding electric field

$$F_{\perp}(\mathbf{r}_i) = \frac{V_S}{4\pi} \int_S d^2r_0 \left[ \frac{6z_h^2}{[r_{i0}^2 + z_h^2]^{5/2}} - \frac{2}{[r_{i0}^2 + z_h^2]^{3/2}} \right], \tag{A.23}$$

which is the positive-definite function for  $\mathbf{r}_i \in S$  and  $V_S \geq 0$ , and zero for  $S$  being the infinite region. Here, the step function  $\theta$  is introduced in Eq. (2.7). Thus, the electrons are confined on the liquid surface by the repulsive exclusion force  $E_{\text{He}}\delta(z_h - z_i)$ , the attractive forces due to the induced charge in the liquid  $^4\text{He}$  and the metal electrodes,  $-\sigma e^2/4(z_i - z_h)^2 - e^2/4z_h^2$ , and the holding field  $-eF_{\perp}(\mathbf{r}_i)$ .

Here, we investigate the motion in the  $z$  direction under the adiabatic approximation for the degree of freedom along the liquid surface. The Hamiltonian of each electron in the  $z$  direction is

$$H_{\perp} = -\frac{\hbar^2}{2m} \frac{\partial^2}{\partial z^2} - \frac{\sigma e^2}{4(z - z_h)} + eF'_{\perp}(z - z_h) + E_{\text{He}}\theta(-z + z_h), \tag{A.24}$$

where  $F'_{\perp} = F_{\perp} + e/4z_h^2$ . Because of  $E_{\text{He}} \sim 1$  eV [73, 76], we can practically approximate  $E_{\text{He}}$  by the infinite barrier  $E_{\text{He}} = \infty$  [72]. Then, we obtain the ground-state energy

$$\langle H_{\perp} \rangle_0 = \frac{\hbar^2 \kappa_0^2}{2m} - \frac{e^2 \kappa_0}{m} + \frac{3eF'_{\perp}}{2\kappa_0}, \tag{A.25}$$

the first-excited-state energy

$$\langle H_{\perp} \rangle_1 = \frac{\hbar^2 \kappa_1^2}{6m} \left[ 1 + \frac{6\kappa_1^2}{\kappa_{01}^2} \right] - \frac{\hbar^2 \kappa_0 \kappa_1}{2m} \left[ 1 + \frac{2\kappa_1^2 - \kappa_0 \kappa_1}{\kappa_{01}^2} \right] + \frac{eF'_{\perp}}{2\kappa_1} \left[ 1 + \frac{4\kappa_0^2 - \kappa_0 \kappa_1 + \kappa_1^2}{\kappa_{01}^2} \right], \tag{A.26}$$

the average distance of the electrons in the ground state

$$\langle z \rangle_0 = \frac{3}{2\kappa_0}, \quad (\text{A.27})$$

and the kinetic energy in the  $z$  direction of the electrons in the ground state

$$\langle K_z \rangle_0 \equiv \left\langle -\frac{\hbar^2}{2m} \frac{\partial^2}{dz^2} \right\rangle_0 = \frac{\hbar^2 \kappa_0^2}{2m}, \quad (\text{A.28})$$

by the variational method with the trial wavefunctions [36, 77]

$$\chi_0(z) = 2\kappa_0^{\frac{3}{2}}(z - z_h)e^{-\kappa_0(z-z_h)}, \quad (\text{A.29})$$

and

$$\chi_1(z) = \frac{2\sqrt{3}\kappa_1^{\frac{5}{2}}}{\kappa_{01}} \left[ 1 - \left\{ \frac{\kappa_0 + \kappa_1}{3} \right\} (z - z_h) \right] (z - z_h)e^{-\kappa_1(z-z_h)}. \quad (\text{A.30})$$

Here,  $\kappa = me^2\sigma/4\hbar^2$  is the inverse of the effective Bohr radius [41],  $\kappa_n$  is the variational parameter to minimize  $\langle H_\perp \rangle_n$ ,  $\kappa_{01} = \kappa_0^2 - \kappa_0\kappa_1 + \kappa_1^2$ , and  $\langle \cdot \rangle_n$  represents the  $n$ th-excited average:

$$\langle \cdot \rangle_n = \int_0^\infty dz \chi_n(z) \cdot \chi_n(z). \quad (\text{A.31})$$

Incidentally, the variational parameter in the ground state is given by [36]

$$\kappa_0 = \frac{3\kappa}{4} \left( \frac{\kappa_\perp}{\kappa} \right)^{\frac{3}{2}} \sinh^{-1} \left[ \frac{1}{3} \operatorname{arcsinh} \left\{ \frac{9}{4} \left( \frac{\kappa_\perp}{\kappa} \right)^{\frac{3}{2}} \right\} \right], \quad (\text{A.32})$$

with

$$\kappa_\perp = \left( \frac{2meF'_\perp}{\hbar^2} \right). \quad (\text{A.33})$$

In Figs. A.3 (a), (b), and (c), we plot  $F_\perp$ , the energy gap  $\Delta H_\perp = \langle H_\perp \rangle_1 - \langle H_\perp \rangle_0$ , and the average distance from the liquid surface  $\Delta z = \langle z \rangle_0 - z_h$  of the electrons in the ground state, across the channel at  $y = 0$  for  $V_S = 0.38$  V and  $z_h = 1.5$   $\mu\text{m}$ . From  $\Delta H_\perp$  and temperature  $T = 1.2$  K, the probability of finding the electrons occupying the first-excited state is  $e^{-\Delta H_\perp/k_B T} \sim 10^{-4} - 10^{-7}$ , and the inter-electron separation  $r_s \sim 10^{-1}$   $\mu\text{m}$  is much larger than the thermal de Broglie wavelength  $\lambda_D \sim 10^{-2}$   $\mu\text{m}$ . Therefore, all electrons occupy the ground state in the independent electron states and thus are located at  $\langle z \rangle_0$ , whereas the parallel motion is classical (see Fig. A.2). We also note that the presumptions  $z_i = z_j$  ( $i \neq j$ ) and  $|z_i - z_h| \ll r_{ij}$ ,  $z_i, z_h$  are valid, and the adiabatic approximation is appropriate because the expected kinetic energy in the  $z$  direction

$$\langle K_z \rangle = \frac{1}{\sum_{n=0}^\infty e^{-\frac{\langle H_\perp \rangle_n}{k_B T}}} \sum_{n=0}^\infty e^{-\frac{\langle H_\perp \rangle_n}{k_B T}} \langle K_z \rangle_n \simeq \langle K_z \rangle_0, \quad (\text{A.34})$$

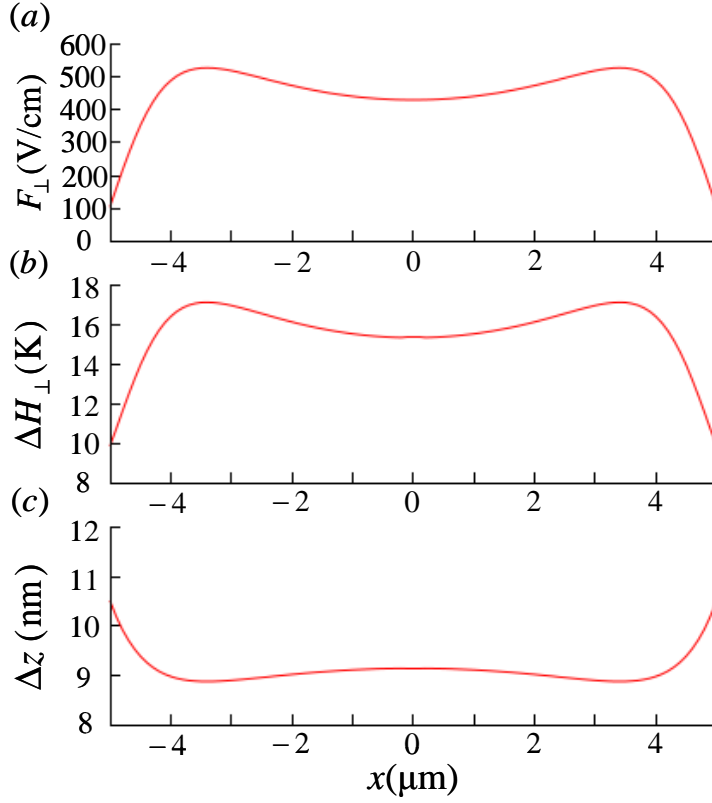


Figure A.3: The holding electric field  $F_{\perp}$  (a), the energy gap  $\Delta H_{\perp}$  between the ground-state and the first excited state (b), and the average distance from the liquid surface  $\Delta z$  of the electrons in the ground state (c), across the channel at  $y = 0$  for  $V_S = 0.38$  V and  $z_h = 1.5$   $\mu\text{m}$ . Under the reported holding field  $F_{\perp} = 6.5 \times 10^2$  V/cm in a very similar device [34] to that used in Ref. [31],  $\Delta H_{\perp}$  is 19 K, and  $\Delta z$  is 8.6 nm.

is of the order of 10 K which is much larger than the classical kinetic energy  $T/2 = 0.6$  K for the parallel motion.

For the difference of the time scale between the vertical and the parallel motion, we can decouple the motion in the  $z$  direction as follows:

$$\begin{aligned}
H_{\parallel} &\simeq \langle H \rangle_0 \\
&= -\frac{\hbar^2}{2m} \sum_{i=1}^N \frac{\partial^2}{\partial \mathbf{r}_i^2} + \sum_{i>j} \left[ \frac{e^2}{r_{ij}} - \frac{e^2}{\sqrt{r_{ij}^2 + 4z_h^2}} + \frac{8e^2\sigma z_h^2}{r_{ij}^3} \right] + eF_{\perp}(\mathbf{r}_i)\Delta z \\
&\quad - \frac{eV_S}{4\pi} \sum_{i=0}^N \int_S d^2r_0 \left[ \frac{(2+\sigma)z_h}{[r_{i0}^2 + z_h^2]^{3/2}} + \frac{3\sigma z_h}{[r_{i0}^2 + 9z_h^2]^{3/2}} \right]. \tag{A.35}
\end{aligned}$$

If we apply the zeroth-order approximation of  $\sigma$  and  $\Delta z$  to  $H_{\parallel}$ ,  $H_{\parallel}$  reduces to

$$\begin{aligned}
H_{\parallel} &= -\frac{\hbar^2}{2m} \sum_{i=1}^N \frac{\partial^2}{\partial \mathbf{r}_i^2} + \sum_{i>j} \left[ \frac{e^2}{r_{ij}} - \frac{e^2}{\sqrt{r_{ij}^2 + 4z_h^2}} \right] \\
&- \frac{eV_S}{4\pi} \sum_{i=0}^N \int_S d^2 r_0 \frac{2z_h}{[r_{i0}^2 + z_h^2]^{3/2}}, \tag{A.36}
\end{aligned}$$

which is the underlying Hamiltonian for the simulation in the body of this thesis. The integration over  $S$  in Eq. (A.36) can be performed exactly if  $S$  consists of rectangles and triangles. The explicit representations are

$$\begin{aligned}
&\int_{X_1}^{X_2} dx_0 \int_{Y_1}^{Y_2} dy_0 \frac{z_h}{[(x-x_0)^2 + (y-y_0)^2 + z_h^2]^{3/2}} \\
&= \arctan \left[ \frac{(x-X_2)(y-Y_2)}{z_h \sqrt{(x-X_2)^2 + (y-Y_2)^2 + z_h^2}} \right] - \arctan \left[ \frac{(x-X_1)(y-Y_2)}{z_h \sqrt{(x-X_1)^2 + (y-Y_2)^2 + z_h^2}} \right] \\
&- \arctan \left[ \frac{(x-X_2)(y-Y_1)}{z_h \sqrt{(x-X_2)^2 + (y-Y_1)^2 + z_h^2}} \right] + \arctan \left[ \frac{(x-X_1)(y-Y_1)}{z_h \sqrt{(x-X_1)^2 + (y-Y_1)^2 + z_h^2}} \right], \tag{A.37}
\end{aligned}$$

for rectangles, and

$$\begin{aligned}
&\int_{X_1}^{X_2} dx_0 \int_{x_0+Y_1-X_1}^{Y_2} dy_0 \frac{z_h}{[(x-x_0)^2 + (y-y_0)^2 + z_h^2]^{3/2}} \\
&= \arctan \left[ \frac{(x-X_2)(y-Y_2)}{z_h \sqrt{(x-X_2)^2 + (y-Y_2)^2 + z_h^2}} \right] - \arctan \left[ \frac{(x-X_1)(y-Y_2)}{z_h \sqrt{(x-X_1)^2 + (y-Y_2)^2 + z_h^2}} \right] \\
&+ \arctan \left[ \frac{\Im\{C_2(x, y)\}}{\Re\{C_2(x, y)\}} \right] - \arctan \left[ \frac{\Im\{C_1(x, y)\}}{\Re\{C_1(x, y)\}} \right], \tag{A.38}
\end{aligned}$$

with

$$C_n(x, y) = \frac{z_h \beta_n - i\alpha \gamma_n}{\alpha^2 \beta_n}, \tag{A.39}$$

$$\alpha(x, y) = x - y + Y_1 - X_1 - iz_h, \tag{A.40}$$

$$\beta_n(x) = x - X_n - iz_h, \tag{A.41}$$

$$\gamma_n(x, y) = X_n - y + Y_1 - X_1 + \sqrt{(x-X_n)^2 + (y-Y_1+X_1-X_n)^2 + z_h^2}, \tag{A.42}$$

for isosceles triangles (see Fig. A.4), where  $\Re\{C\}$  and  $\Im\{C\}$  represent the real and the imaginary parts of the complex number  $C$ , respectively.

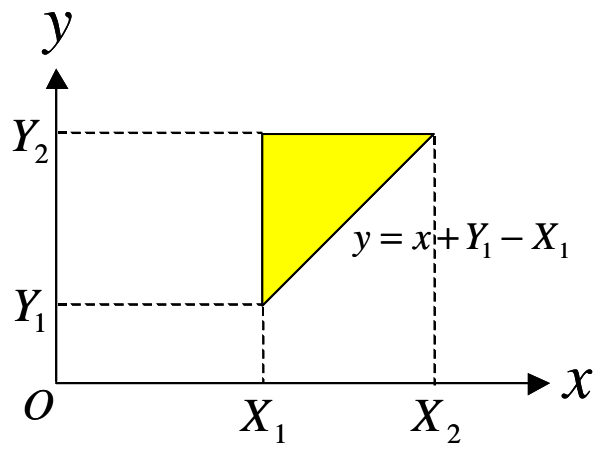


Figure A.4: The integration range for a isosceles triangle in Eq. (A.38).

## A.4 Regarding of the difference between our model and the device structure

In this subsection, we show the difference between our model and the device structure in the experiment [31], and discuss the change of electric potential due to the difference. We depict the structures of our model and the device in Figs A.5 (a) and (b) respectively. From the distinction of the position of the guard electrodes, it may be assumed that the screening effect between electrons, the confining field, and the holding field for our system are weaker than those for the device. However, we cannot explicitly obtain electric potential from the Poisson equation with such complex boundary conditions. On the other hand, the arrangement of the gate electrodes for our system is almost similar to that for the device structure [31]. Therefore, we believe that the electric field by the point contact in our system reproduces that in the device.

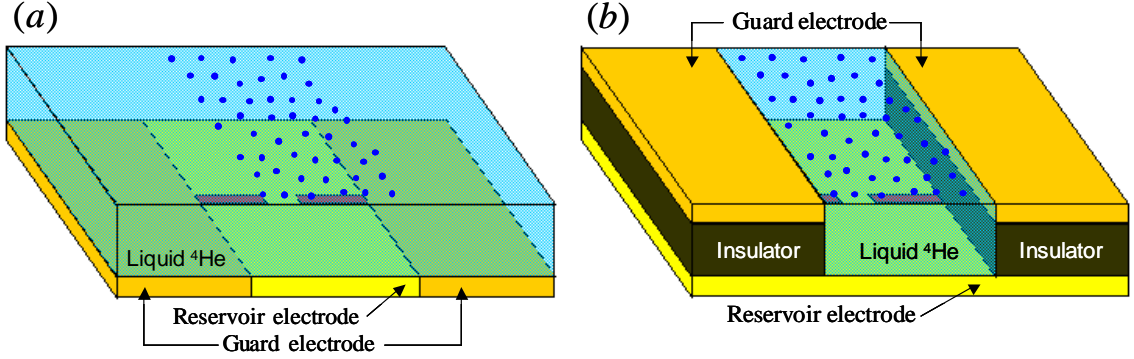


Figure A.5: (a) The structure of the channel in our model. In the model, the reservoir, the guard, and the gate electrodes are placed at the same plane, where the two red regions in the center of the reservoir electrode correspond to the gate electrodes. On the plane, liquid  $^4\text{He}$  fills over the whole. (b) The structure of the channel in the device in the experiment [31]. In the device, the reservoir and the gate electrodes are placed at the same plane, where the two gate electrodes are indicated by the red regions in the center of the reservoir electrode. On the other hand, the guard electrodes fixed on the insulators are placed on the plane apart from each other by the channel width. The formed hollow by the fixing of the guard electrodes is filled with liquid  $^4\text{He}$ .



# Appendix B

## 2D electron transport over liquid $^4\text{He}$ in idealized geometry

In this appendix, we investigate 2D electron transport over liquid  $^4\text{He}$  on metal electrodes. Based on the analysis, we estimate transport coefficients for the electrons in idealized geometry of the device structure [31].

### B.1 Bulk 2D electron transport over liquid $^4\text{He}$ on metal electrodes

In this subsection, we investigate the transport process for bulk 2D electron systems over liquid  $^4\text{He}$  on metal electrodes. For  $z_{\text{He}} \sim 1 \mu\text{m}$  and  $T \sim 1 \text{ K}$ , the electrons in the system are scattered by helium gas atoms, and ripples [29, 35, 41]. We first calculate the effective collision frequencies, which are defined by the relaxation time in the Drude formula, with the known kinetic theory under the single electron (SE) approximation [28, 29, 35, 41]. The frequency under the theory is given in Ref. [46] as

$$\frac{1}{\nu^{\text{se}}} = \int_0^\infty dx \frac{x e^{-x}}{\nu_{\text{eg}} + \nu_{\text{er}}^{\text{se}}(x)}, \quad (\text{B.1})$$

with the collision frequency of the electron-helium gas atom collisions [41]

$$\nu_{\text{eg}} = \frac{3\pi^2 a_{\text{He}}^2 \hbar n_{\text{g}} \kappa_0}{2m}, \quad (\text{B.2})$$

and the collision frequency of the electron-ripple collisions [46]

$$\nu_{\text{er}}^{\text{se}}(x) \simeq \frac{e^2}{4\hbar\alpha} \left[ F_p^2 + \frac{4\sqrt{2}}{\pi} \frac{F_p F_\perp}{\sqrt{x}} + \frac{F_\perp^2}{x} \right]. \quad (\text{B.3})$$

Here,  $a_{\text{He}}$  is the scattering length of  $^4\text{He}$ ,  $n_{\text{g}} = (Mk_{\text{B}}T/2\pi\hbar^2)^{3/2} \exp(-E_{\text{He}}/k_{\text{B}}T)$  is volume concentration of helium atom with the vaporization energy  $E_{\text{He}}$  and the

${}^4\text{He}$  mass  $M$ ,  $F_p = e\sigma\kappa_0\sqrt{mk_B T}/(6\hbar)$ , and  $\alpha$  is the surface tension of liquid  ${}^4\text{He}$ . From Eqs. (B.1)-(B.3) and the material constants of  ${}^4\text{He}$  in Table B.1, we obtain  $\nu^{\text{se}} \approx 7.2 \times 10^9 \text{ s}^{-1}$  for  $F_\perp = 6.5 \times 10^2 \text{ V/cm}$ , and  $\nu^{\text{se}} \approx 4.4 \times 10^9 \text{ s}^{-1}$  for  $F_\perp = 0 \text{ V/cm}$ .

Table B.1: Material constants of  ${}^4\text{He}$  [41].

$a_{\text{He}}$	=	6.1	×	$10^{-9}$	cm
$M$	=	6.65	×	$10^{-24}$	g
$E_{\text{He}}$	=	9.90	×	$10^{-16}$	erg
$\alpha$	=	3.7	×	10	dyn/cm

On the other hand, the electron-electron (EE) collision frequency [46, 78]

$$\nu_{\text{ee}} = 2.1 \bar{n}_{\text{E}}^{3/4} \sqrt{e^2/m} \approx 2.5 \times 10^{11} \text{ s}^{-1}, \quad (\text{B.4})$$

for the density  $\bar{n}_{\text{E}} = 1.5 \times 10^9 \text{ cm}^{-2}$  in Ref. [31] is much larger than  $\nu^{\text{se}}$ . In the complete control region  $\nu_{\text{ee}} \gg \nu^{\text{se}}$ , the momentum relaxation of the electron distribution is governed by the EE collisions; accordingly the equilibrium distribution function  $\Psi_0(E_v/k_B T)$  is shifted to the direction of the drift velocity  $\mathbf{v}_{\text{D}}$  as follows:  $\Psi_0^{\text{cc}}[(E_v - m\mathbf{v} \cdot \mathbf{v}_{\text{D}})/k_B T_e]$ , where  $E_v = mv^2/2$  is the kinetic energy, and  $T_e$  is the effective temperature of electrons [42–46]. We can also approximate  $T_e \simeq T$  because of  $T_e - T \ll 1$  for the weak driving field in the systems we treat [41]. From the kinetic equation based on this treatment, which is called by the complete control (CC) approximation, we obtain the effective collision frequency as

$$\nu^{\text{cc}} = \nu_{\text{eg}} + \nu_{\text{er}}^{\text{cc}}. \quad (\text{B.5})$$

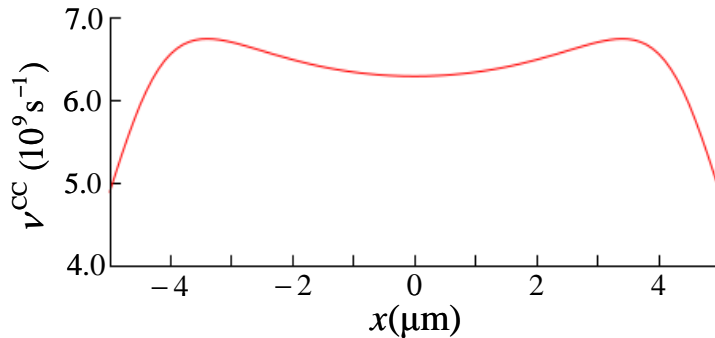


Figure B.1: The effective collision frequency  $\nu^{\text{cc}}$  across the channel at  $y = 0$  under the holding field  $F_\perp$  in Eq. (A.23) [Fig. A.3 (a)] and  $\kappa_0$  in Eq. (A.32) for  $V_S = 0.38 \text{ V}$  and  $z_h = 1.5 \mu\text{m}$ . Under the reported holding field  $F_\perp = 6.5 \times 10^2 \text{ V/cm}$  in Ref. [34],  $\nu^{\text{cc}}$  is  $7.3 \times 10^9 \text{ s}^{-1}$ .

with [46]

$$\nu_{\text{er}}^{\text{cc}} \simeq \frac{e^2}{4\hbar\alpha} \left[ F_p^2 + \frac{4}{\sqrt{2\pi}} F_p F_\perp + F_\perp^2 \right]. \quad (\text{B.6})$$

In Fig. B.1, we plot  $\nu^{\text{cc}}$  across the channel at  $y = 0$  under the holding field  $F_\perp$  in Eq. (A.23) [see Fig. A.3 (a)]. Under the reported holding field  $F_\perp = 6.5 \times 10^2$  V/cm in Ref. [34],  $\nu^{\text{cc}}$  is  $7.3 \times 10^9$  s $^{-1}$ .

To obtain the value of the mean free path

$$l_m = \frac{v_D}{\nu^{\text{cc}}} = \frac{e}{m} \frac{F_\parallel}{[\nu^{\text{cc}}]^2}, \quad (\text{B.7})$$

we estimate the driving field  $F_\parallel$  for the experiment [31]. As seen in Fig. C.1,  $F_\parallel$  is induced by the applied voltage between the left and the right reservoir electrode. We can imitate the field by changing the boundary conditions for  $\phi_C$  in Eq. (2.5) as follows:

$$\begin{aligned} \phi_C^{\text{D}}(\mathbf{r}; V_L, V_R) &= -\frac{eV_L}{4\pi} \int_{\bar{S}_L} dx_0 dy_0 \left[ \frac{2z_h}{[|\mathbf{r} - \mathbf{r}_0|^2 + z_h^2]^{3/2}} \right] \\ &\quad - \frac{eV_R}{4\pi} \int_{\bar{S}_R} dx_0 dy_0 \left[ \frac{2z_h}{[|\mathbf{r} - \mathbf{r}_0|^2 + z_h^2]^{3/2}} \right], \end{aligned} \quad (\text{B.8})$$

where  $\bar{S}_L$  and  $\bar{S}_R$ , respectively, represent the left and the right reservoir electrodes (see Fig. B.2), and  $V_L$  and  $V_R$  are the applied voltage to  $\bar{S}_L$  and  $\bar{S}_R$ , respectively. Using  $\phi_C^{\text{D}}$ , we define the effective driving field as

$$F_\parallel(\mathbf{r}) = \frac{1}{e} \left| \frac{\partial \phi_C^{\text{D}}(\mathbf{r}; V_0 - \Delta V, V_0)}{\partial y} - \frac{\partial \phi_C^{\text{D}}(\mathbf{r}; V_0, V_0)}{\partial y} \right| \quad (\text{B.9})$$

where  $\Delta V = 2.0$  mV is the applied voltage in the experiment [31]. The average value of  $F_\parallel(x, y)$  over  $-D \leq y \leq D$  at  $x = 0$  is 0.57 V/cm, which leads to  $l_m \approx 0.19$   $\mu\text{m}$ . Therefore, the system is diffusive [5–11].

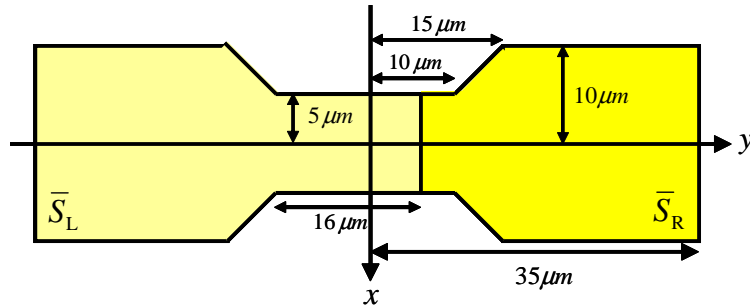


Figure B.2: The boundary condition at  $z = 0$  for  $\phi_C^{\text{D}}$ :  $\bar{S}_L$  and  $\bar{S}_R$  are, respectively, the light yellow and yellow regions. The electric potential in  $\bar{S}_L$  and  $\bar{S}_R$  are  $V_L$  and  $V_R$ , respectively.

## B.2 Estimation of conductance for the electrons in idealized channel geometry

In this section, we calculate transport coefficients (TC) for the electron system in idealized geometry of the device structure [31]. In diffusive regions under weak driving field, the relaxation of electron distribution is realized within much smaller spatial extent than the scale of the geometry. Therefore, we can adopt the linear relation  $\mathbf{j}_{\parallel}(\mathbf{r}) = \sigma(\mathbf{r})\mathbf{F}_{\parallel}(\mathbf{r})$  with the conductivity  $\sigma(\mathbf{r}) = n(\mathbf{r})e^2/m\nu^{\text{cc}}(\mathbf{r})$  which consists of the density  $n(\mathbf{r})$  and the derived frequency  $\nu^{\text{cc}}(\mathbf{r})$  from the bulk kinetic equation at each position on the liquid surface [11]. Here,  $\mathbf{j}_{\parallel}(\mathbf{r})$  is the current density in the surface direction at  $\mathbf{r}$ . We also ignore the dependence of  $\sigma$  on space, and set  $n(\mathbf{r}) \simeq \bar{n}_{\text{E}}$  and  $\nu^{\text{cc}}(\mathbf{r}) \simeq 7.3 \times 10^9 \text{ s}^{-1}$ , namely disregards the gradual variation of electric potential as seen in Fig. 2.2 (c) and Ref. [31]. In Fig. B.3 (a), we depict channel geometry defined by ideal hard walls, with bottlenecks and a gate, which is the

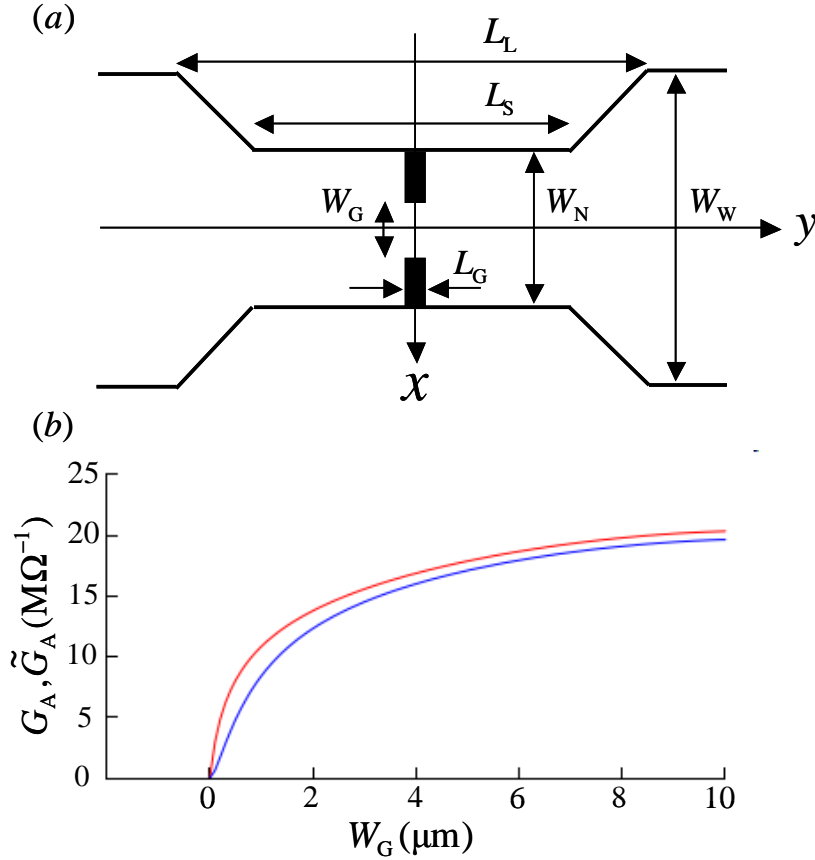


Figure B.3: (a) The idealized channel geometry with the bottlenecks and the gate. The channel is defined by only ideal hard walls. (b) The conductance  $G_A$  and  $\tilde{G}_A$  as a function of  $W_G$  under the parameters:  $L_L = 30\mu\text{m}$ ,  $L_S = 20\mu\text{m}$ ,  $L_G = 1.4\mu\text{m}$ ,  $W_W = 20\mu\text{m}$ , and  $W_N = 10\mu\text{m}$ .

idealized geometry of the device structure [31]. In the following, we call the portion of  $-L_L/2 \leq y \leq L_L/2$ ,  $L_S/2 \leq |y| \leq L_L/2$ , and  $-L_G/2 \leq y \leq L_G/2$ , respectively, the channel, the bottleneck, and the gate. Here,  $L_L$  and  $L_S$  are, respectively, the length of the channel with and without the bottlenecks, and  $L_G$  is the length of the gate.

Based on the Poisson equation in the geometry and the Ohm's law, the resistance for the bottlenecks and the gate is calculated in Ref. [53] as

$$R_B(\rho) = \frac{\rho}{\pi} \left\{ \frac{W_W^2 + W_N^2}{W_W W_N} \operatorname{arctanh} \left[ \frac{W_N}{W_W} \right] + \frac{W_W^2 - W_N^2}{W_W W_N} \operatorname{arctan} \left[ \frac{W_N}{W_W} \right] + \log \left[ \frac{W_W^4 - W_N^4}{8W_W^2 W_N^2} \right] \right\}, \quad (\text{B.10})$$

and

$$R_G(\rho, W_G) = \rho \frac{L_G}{W_G} + \frac{\rho}{\pi} \left\{ \frac{W_N^2 + W_G^2}{W_N W_G} \log \left[ \frac{W_N + W_G}{W_N - W_G} \right] + 2 \log \left[ \frac{W_N^2 - W_G^2}{4W_N W_G} \right] \right\}, \quad (\text{B.11})$$

respectively. Here,  $\rho$  is the resistivity,  $W_N$  and  $W_W$  are, respectively, the widths at the narrow and the wide section of the bottleneck, and  $W_G$  is the gap width of the gate. Therefore, the resistance in the channel is given by

$$R_A(W_G) = \rho_0 \frac{L_S - L_G}{W_N} + 2R_B(\rho_0) + R_G(\rho_0, W_G), \quad (\text{B.12})$$

where  $\rho_0 = m\nu^{\text{cc}}/\bar{n}_E e^2$ .

In addition, we take into account the change of microscopic TC due to the existence of hard-wall boundaries with the boundary scattering theory [1, 79–84]. We calculate the correction of  $\nu^{\text{cc}}$  with the Boltzmann equation under the first order approximation of an in-plane driving field  $F_{\parallel}$  and a deviation of an electron distribution function,  $\Psi_1$ , from an equilibrium electron distribution function  $\Psi_0$ . Here,  $\Psi_0$  is the product of an equilibrium density distribution function and the Maxwell-Boltzmann distribution function  $M(v)$ . Applying  $F_{\parallel}$  in the  $y$  axis direction, the equation is given by [19, 20, 80]

$$\mathbf{v} \cdot \frac{\partial \Psi_1(\mathbf{r}, \mathbf{v})}{\partial \mathbf{r}} - \frac{eF_{\parallel}}{m} \frac{\partial \Psi_0(v)}{\partial v_y} = -\nu^{\text{cc}} \Psi_1(\mathbf{r}, \mathbf{v}), \quad (\text{B.13})$$

which can be solved under the channel geometry defined by hard walls at  $x = W/2$  and  $x = -W/2$ . We assume inelastic electron scattering at the boundaries, which is called by the diffusive boundary scattering [79, 80]. Then,  $\Psi_1$  is explicitly given by

$$\Psi_1(\mathbf{r}, \mathbf{v}) = \frac{eF_{\parallel} v_y}{\nu^{\text{cc}} k_B T} M(v) \times \begin{cases} [1 - e^{-\nu^{\text{cc}}(x+W)/v_x}] & (v_x \geq 0) \\ [1 - e^{-\nu^{\text{cc}}(x-W)/v_x}] & (v_x < 0). \end{cases} \quad (\text{B.14})$$

Therefore, we obtain the corrected collision frequency as follows:

$$\tilde{\nu}^{\text{cc}}(W) = \nu^{\text{cc}} / \left\{ 1 - \frac{v_{\text{th}}}{\sqrt{\pi} \nu^{\text{cc}} W} + \frac{v_{\text{th}}}{\sqrt{\pi} \nu^{\text{cc}} W} 2 \int_0^{\infty} d\eta \exp \left[ - \left( \eta^2 + \frac{\nu^{\text{cc}} W}{v_{\text{th}}} \frac{1}{\eta} \right) \right] \right\}, \quad (\text{B.15})$$

where  $v_{\text{th}} = \sqrt{2k_{\text{B}}T/m}$  is the thermal velocity. We define the resistance under this correction as

$$\tilde{R}_{\text{A}}(W_{\text{G}}) = \rho(W_{\text{N}}) \frac{L_{\text{S}} - L_{\text{G}}}{W_{\text{N}}} + 2R_{\text{B}}[\rho(W_{\text{W}})] + R_{\text{G}}[\rho(W_{\text{G}}), W_{\text{G}}], \quad (\text{B.16})$$

where  $\rho(W) = m\tilde{\nu}^{\text{cc}}(W)/\bar{n}_{\text{E}}e^2$ . For the resistivity in  $R_{\text{B}}$  in Eq. (B.16), we simply adopt  $W_{\text{W}}$  as the channel width.

In Fig. B.3 (b), we plot the conductance  $G_{\text{A}} = 1/R_{\text{A}}$  and  $\tilde{G}_{\text{A}} = 1/\tilde{R}_{\text{A}}$  as a function of  $W_{\text{G}}$  under the parameters:

$$\begin{aligned} L_{\text{L}} &= 30 \quad \mu\text{m}, \\ L_{\text{S}} &= 20 \quad \mu\text{m}, \\ L_{\text{G}} &= 1.4 \quad \mu\text{m}, \\ W_{\text{W}} &= 20 \quad \mu\text{m}, \\ W_{\text{N}} &= 10 \quad \mu\text{m}. \end{aligned} \quad (\text{B.17})$$

In the comparison between  $G_{\text{A}}$  and the experimental resistance  $G_{\text{E}}$  [31],  $G_{\text{A}}$  is about 10 times larger than  $G_{\text{E}}$ . Although the qualitative behavior between them is similar, it is not clear whether the linear relation between  $W_{\text{G}}$  and  $V_{\text{G}}$  is established. In the comparison between  $\tilde{G}_{\text{A}}$  and  $G_{\text{A}}$ ,  $\tilde{G}_{\text{A}}$  is almost similar to  $G_{\text{A}}$ , and thus, the boundary scattering effect little affect the channel conductance. For these results, we suppose that both of the non-uniformity by the external potential and the electron correlations are essential to reproduce the value of and the steplike structure in  $G_{\text{E}}$ .

# Appendix C

## Details on molecular dynamics simulation method

In this appendix, we give the reason to select constant temperature molecular dynamics (CTMD) with Nosé-Hoover thermostat and constant chemical potential molecular dynamics (CCMD) to investigate dynamics of the electrons in the experiment, with the comparison between our method and the experimental setup [31]. In addition, we propose new grand canonical ensemble molecular dynamics, though the method is not used for the calculation results in this thesis.

### C.1 Reason to select constant temperature and chemical potential molecular dynamics

In this subsection, we explain why we select CTMD with Nosé-Hoover thermostat and CCMD to investigate the transport of the electrons in the experiment. The CTMD we adopt is the established one to reproduce the precise equilibrium state [55–57]. The equations of motions in the CTMD are given by [57]

$$m \frac{d^2 r_i^\alpha}{dt^2} = - \sum_{j(\neq i)} \frac{\partial \phi_I(r_{ij})}{\partial r_i^\alpha} - \frac{\partial \phi_C(\mathbf{r}_i)}{\partial r_i^\alpha} - m \dot{\zeta} \dot{r}_i^\alpha, \quad (\text{C.1})$$

$$Q_\zeta \frac{d^2 \zeta}{dt^2} = 2 \left[ \sum_i \frac{m \dot{r}_i^2}{2} - \frac{g k_B T_K}{2} \right], \quad (\text{C.2})$$

where  $g$  is the number of degree of freedom of the system. These equations are derived from the Hamiltonian

$$\tilde{H}_T = \sum_i \frac{\tilde{p}_i^2}{2m s^2} + \sum_{i>j} \phi_I(r_{ij}) + \sum_i \phi_C(\mathbf{r}_i) + \frac{p_s^2}{2Q_\zeta} + g k_B T_K \log s, \quad (\text{C.3})$$

under the transformations:  $\tilde{\mathbf{p}}_i/s = \mathbf{p}_i = m \dot{\mathbf{r}}_i$ ,  $d\tilde{t}/s = dt$ , and  $\log s = \zeta$ . Here,  $\tilde{\mathbf{p}}_i$ ,  $s$ ,  $p_s$ , and  $\tilde{t}$  are, respectively, the conjugate momentum of  $\mathbf{r}_i$ , an involved variable

with temperature control, the conjugate momentum of  $s$ , and time, for the extended system described by  $\dot{H}^T$ . On the trajectory along the time evolutions described by Eqs. (C.1) and (C.2),  $H_T$  is conserved, and moreover, we can obtain the canonical ensemble average of any physical quantity as the trajectory is ergodic [57].

We select the chemical-potential gradient by the chemical-potential difference between two reservoirs as the driving field to imitate the inhomogeneous electric field and the huge reservoirs in the experiment [31] (see Sec. 2.3. In Fig. C.1, we depict the setup in the experiment in which the driving field is a time- and space-dependent field induced by the applied voltage between the left and the right reservoir electrode under liquid  $^4\text{He}$ . First, in spite of the dependence of it on time for the experiment, we select the driving field independent on time. This is because the cycles applied in the experiment [31],  $5.0 \times 10^{-6}$  s, corresponding to  $10^7$  steps of our MD are too long. Next, we give the formal connection of the driving field between our MD and the experiment. In our MD, the equations of motion for the electrons in the channel can be represented as

$$m \frac{d^2 r_i^\alpha}{dt^2} = - \sum_{j(\neq i) \in S_C} \frac{\partial \phi_I(r_{ij})}{\partial r_i^\alpha} - \frac{\partial \phi_C(\mathbf{r}_i)}{\partial r_i^\alpha} - m \dot{\zeta} \dot{r}_i^\alpha - \frac{\partial \phi_D(\mathbf{r}_i)}{\partial r_i^\alpha}, \quad (\text{C.4})$$

$$Q_\zeta \frac{d^2 \zeta}{dt^2} = 2 \left[ \sum_i \frac{m \dot{r}_i^2}{2} - N k_B T_K \right], \quad (\text{C.5})$$

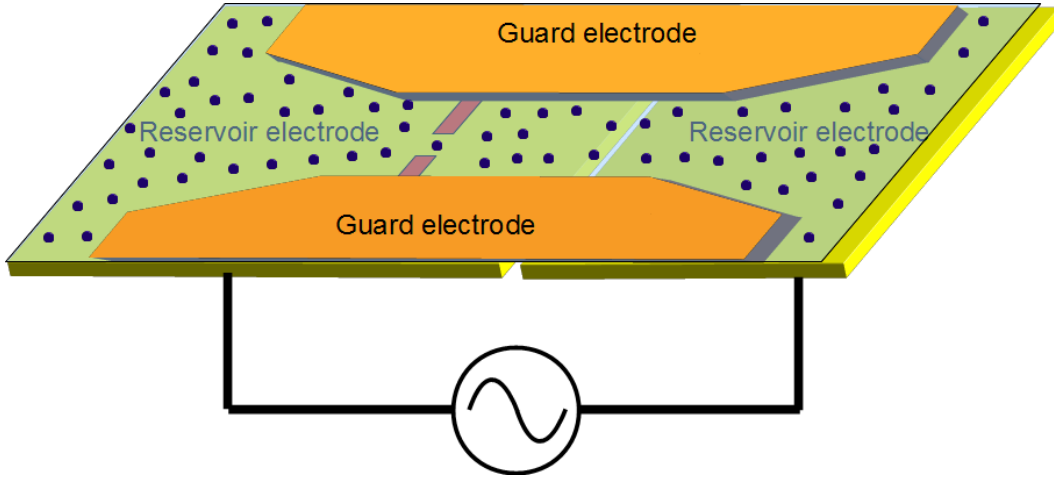


Figure C.1: A schematic view to explain what driving field is used in the experiment [31]. In the experiment, an alternative voltage is applied between two electrodes under liquid  $^4\text{He}$ . The arrangement of the two reservoir electrodes is asymmetric with regard to the center of the channel. Here, the two red regions under liquid  $^4\text{He}$  indicate the arrangement of the gate electrode, and the blue circles represent electrons. The size of each reservoir is about a hundred longer than the channel.

where  $S_C = \{(x, y) | -D < y < D\}$  is the region of the channel, and

$$\phi_D(\mathbf{r}_i) = \sum_{j \in S_L} \phi_I(r_{ij}) + \sum_{j \in S_R} \phi_I(r_{ij}), \quad (\text{C.6})$$

is the potential due to the electrons in the left and the right reservoirs (see Eqs. (2.7) and (2.8) in Sec. 2.3). For the state  $\mu_L > \mu_R$ ,  $\phi_D$  generates the gradient of the electric potential to the channel. Thus, the chemical-potential difference has an effect similar to the inhomogeneous electric potential formally. In addition, the reservoirs with the varying number of particles is also to imitate the huge reservoirs in the experiment [31].

To introduce the chemical-potential difference, we select CCMD instead of the grand canonical ensemble MD (GCMD) [58, 61] because the equations of motion of GCMD include to a factor making the system unstable. The equations of motion in CCMD we adopt are given by

$$m \frac{d^2 r_i^\alpha}{dt^2} = - \sum_{j(\neq i)} \frac{\partial \phi_I(r_{ij})}{\partial r_i^\alpha} - \frac{\partial \phi_C(\mathbf{r}_i)}{\partial r_i^\alpha} - (\nu - N) \frac{\partial \phi_I(r_{if})}{\partial r_i^\alpha}, \quad (\text{C.7})$$

$$m \frac{d^2 r_f^\alpha}{dt^2} = -(\nu - N) \left[ \sum_i \frac{\partial \phi_I(r_{if})}{\partial r_f^\alpha} + \frac{\partial \phi_C(\mathbf{r}_f)}{\partial r_f^\alpha} \right], \quad (\text{C.8})$$

$$Q_\nu \frac{d^2 \nu}{dt^2} = \mu^1 - \sum_i \phi_I(r_{if}) - \phi_C(\mathbf{r}_f), \quad (\text{C.9})$$

which are derived from the Hamiltonian

$$\begin{aligned} H_C = & \sum_i \frac{p_i^2}{2m} + \sum_{i>j} \phi_I(r_{ij}) + \sum_i \phi_C(\mathbf{r}_i) \\ & + \frac{p_f^2}{2m} + (\nu - N) \left[ \sum_i \phi_I(r_{if}) + \phi_C(\mathbf{r}_f) \right] + \frac{p_\nu^2}{2Q_\nu} - U_\nu. \end{aligned} \quad (\text{C.10})$$

Here,  $\mathbf{r}_f$  is the position of the fractional particle,  $\mathbf{p}_f$  is the conjugate momentum of  $\mathbf{r}_f$ ,  $\nu$  is the ENV,  $p_\nu$  is the conjugate momentum of  $\nu$ , and the potential energy for ENV is represented as follows:

$$U_\nu = N(\mu^0 + \mu^1) + k_B T \log \left[ \frac{\lambda_D^2}{A_S} \right] + (\nu - N)\mu^1, \quad (\text{C.11})$$

with the ideal part  $\mu^0$  and the excess part  $\mu^1$  of the chemical potential  $\mu$ , and the system area  $A_S$ . On the other hand, the equations of motion of GCMD are given

by

$$m \frac{d^2 r_i^\alpha}{dt^2} = - \sum_{j(\neq i)} \frac{\partial \phi_I(r_{ij})}{\partial r_i^\alpha} - \frac{\partial \phi_C(\mathbf{r}_i)}{\partial r_i^\alpha} - (\nu - N) \frac{\partial \phi_I(r_{if})}{\partial r_i^\alpha} - m \dot{\zeta} \dot{r}_i^\alpha, \quad (\text{C.12})$$

$$m \frac{d^2 r_f^\alpha}{dt^2} = -(\nu - N) \left[ \sum_i \frac{\partial \phi_I(r_{fi})}{\partial r_f^\alpha} + \frac{\partial \phi_C(\mathbf{r}_f)}{\partial r_f^\alpha} \right] - m \dot{\zeta} \dot{r}_f^\alpha, \quad (\text{C.13})$$

$$Q_\zeta \frac{d^2 \zeta}{dt^2} = 2 \left[ \sum_i \frac{m \dot{r}_i^2}{2} + \frac{m \dot{r}_f^2}{2} - \frac{g k_B T_K}{2} \right], \quad (\text{C.14})$$

$$Q_\nu \frac{d^2 \nu}{dt^2} = e^{2\zeta} \left[ \mu^1 - \sum_i \phi_I(r_{fi}) - \phi_C(\mathbf{r}_f) \right] - Q_\nu \dot{\zeta} \dot{\nu}, \quad (\text{C.15})$$

which are derived from the Hamiltonian

$$\begin{aligned} \tilde{H}_G = & \sum_i \frac{\tilde{p}_i^2}{2ms^2} + \sum_{i>j} \phi_I(r_{ij}) + \sum_i \phi_C(\mathbf{r}_i) + \frac{p_s^2}{2Q_\zeta} + g k_B T_K \log s \\ & + \frac{\tilde{p}_f^2}{2ms^2} + (\nu - N) \left[ \sum_i \phi_I(r_{fi}) + \phi_C(\mathbf{r}_f) \right] + \frac{p_\nu^2}{2Q_\nu} - U_\nu, \end{aligned} \quad (\text{C.16})$$

under the transformations:  $\tilde{\mathbf{p}}_i/s = \mathbf{p}_i = m\dot{\mathbf{r}}_i$ ,  $\tilde{\mathbf{p}}_f/s = \mathbf{p}_f = m\dot{\mathbf{r}}_f$ ,  $d\tilde{t}/s = dt$ , and  $\log s = \zeta$ . In comparison between Eq. (C.9) and Eq. (C.15), the latter equation is dependent on  $\zeta$ . In non-equilibrium steady states, this brings the system unstable because  $\zeta$  increases with time.

To demonstrate the increase, we consider the simulation with GCMD instead of our MD with CCMD (see Sec. 2.3). In the simulation with GCMD, a rate of change in the internal energy including to the contribution of the fractional particles is given by

$$\begin{aligned} \frac{dH_0}{dt} = & \frac{d}{dt} \left[ \sum_i \frac{m \dot{r}_i^2}{2} + \sum_{i>j} \phi_I(r_{ij}) + \sum_i \phi_C(\mathbf{r}_i) \right. \\ & \left. + \sum_{\gamma=L,R} \left\{ \frac{m \dot{r}_\gamma^2}{2} + (\nu_\gamma - N_\gamma) \sum_i \phi_I(r_{\gamma i}) + \phi_C(\mathbf{r}_\gamma) \right\} \right] \\ = & \sum_i m \dot{\mathbf{r}}_i \cdot \ddot{\mathbf{r}}_i + \sum_{i \neq j} \dot{\mathbf{r}}_i \cdot \frac{\partial \phi_I(r_{ij})}{\partial \mathbf{r}_i} + \sum_i \dot{\mathbf{r}}_i \cdot \frac{\partial \phi_C(\mathbf{r}_i)}{\partial \mathbf{r}_i} \\ & + \sum_{\gamma=L,R} \left[ m \dot{\mathbf{r}}_\gamma \cdot \ddot{\mathbf{r}}_\gamma + \dot{\nu}_\gamma \left\{ \sum_{i \in S_\gamma} \phi_I(r_{\gamma i}) + \phi_C(\mathbf{r}_\gamma) \right\} \right. \\ & \left. + (\nu_\gamma - N_\gamma) \left\{ \sum_{i \in S_\gamma} \dot{\mathbf{r}}_\gamma \cdot \frac{\partial \phi_I(r_{\gamma i})}{\partial \mathbf{r}_\gamma} + \sum_{i \in S_\gamma} \dot{\mathbf{r}}_i \cdot \frac{\partial \phi_I(r_{\gamma i})}{\partial \mathbf{r}_i} + \dot{\mathbf{r}}_\gamma \cdot \frac{\partial \phi_C(\mathbf{r}_\gamma)}{\partial \mathbf{r}_\gamma} \right\} \right], \end{aligned} \quad (\text{C.17})$$

which is about zero for steady states. From Eqs. (C.12) and (C.13), the rate reduces to

$$\frac{dH_0}{dt} = -2\dot{\zeta} \left[ \sum_i \frac{m\dot{\mathbf{r}}_i^2}{2} + \sum_{\gamma=L,R} \frac{m\dot{\mathbf{r}}_\gamma^2}{2} \right] + \sum_{\gamma=L,R} \dot{\nu}_\gamma \left\{ \sum_i \phi_I(r_{\gamma i}) + \phi_C(\mathbf{r}_\gamma) \right\}. \quad (\text{C.18})$$

In Eq. (C.18), the kinetic energy in the bracket  $[\dots]$  of the right-hand side is roughly constant for constant temperature, and the sum over  $\gamma = L, R$  of the right-hand side is non-zero and positive because  $\dot{\nu}_L \simeq -\dot{\nu}_R$  and  $[\sum_i \phi_I(r_{Li}) + \phi_C(\mathbf{r}_L)] > [\sum_i \phi_I(r_{Ri}) + \phi_C(\mathbf{r}_R)]$  for  $\mu_L^1 > \mu_R^1$ , i.e.,

$$\begin{aligned} \sum_{\gamma=L,R} \dot{\nu}_\gamma \left\{ \sum_i \phi_I(r_{\gamma i}) + \phi_C(\mathbf{r}_\gamma) \right\} \\ \simeq \dot{\nu}_L \left[ \left\{ \sum_i \phi_I(r_{Li}) + \phi_C(\mathbf{r}_L) \right\} - \left\{ \sum_i \phi_I(r_{Ri}) + \phi_C(\mathbf{r}_R) \right\} \right] > 0. \end{aligned} \quad (\text{C.19})$$

Therefore,  $\dot{\zeta}$  is also non-zero and positive, and thus  $\zeta$  increases with time, which also imply that the work to remove the electron with low potential energy and to insert the electron with high potential energy accumulates to  $\zeta$  as the heat  $gk_B T_K \zeta$ . Thus, we cannot adopt GCEMD to simulate the system in non-equilibrium steady states.

## C.2 New grand canonical ensemble molecular dynamics

In this subsection, we propose the new Hamiltonian for GCEMD. The equations of motion derived from the new Hamiltonian do not include the problematic factor for our purpose. The new Hamiltonian we propose is

$$\begin{aligned} \tilde{H}_{\text{NG}} = & \sum_i \frac{\tilde{p}_i^2}{2ms^2} + \sum_{i>j} \phi_I(r_{ij}) + \sum_i \phi_C(\mathbf{r}_i) + \frac{p_s^2}{2Q_\zeta} + gk_B T_K \log s \\ & + \frac{\tilde{p}_f^2}{2ms^2} + (\nu - N) \left[ \sum_i \phi_I(r_{if}) + \phi_C(\mathbf{r}_f) \right] + \frac{\tilde{p}_\nu^2}{2Q_\nu s^2} - U_\nu, \end{aligned} \quad (\text{C.20})$$

where  $\tilde{p}_\nu$  is the conjugate momentum of  $\nu$  in the extended system described by  $\tilde{H}^{NG}$ . In the virtual phase space for the extended system, the equations of motion are

obtained through canonical equations as

$$\frac{\partial \mathbf{r}_i}{\partial \tilde{t}} = \frac{\tilde{\mathbf{p}}_i}{ms^2}, \quad (\text{C.21})$$

$$\frac{\partial \tilde{\mathbf{p}}_i}{\partial \tilde{t}} = - \sum_{j(\neq i)} \frac{\partial \phi_{\text{I}}(r_{ij})}{\partial \mathbf{r}_i} - \frac{\partial \phi_{\text{C}}(\mathbf{r}_i)}{\partial \mathbf{r}_i} - (\nu - N) \frac{\partial \phi_{\text{I}}(r_{if})}{\partial \mathbf{r}_i}, \quad (\text{C.22})$$

$$\frac{\partial \mathbf{r}_f}{\partial \tilde{t}} = \frac{\tilde{\mathbf{p}}_f}{ms^2}, \quad (\text{C.23})$$

$$\frac{\partial \tilde{\mathbf{p}}_f}{\partial \tilde{t}} = -(\nu - N) \left[ \sum_i \frac{\partial \phi_{\text{I}}(r_{fi})}{\partial \mathbf{r}_f} - \frac{\partial \phi_{\text{C}}(\mathbf{r}_f)}{\partial \mathbf{r}_f} \right], \quad (\text{C.24})$$

$$\frac{\partial s}{\partial \tilde{t}} = \frac{p_s}{Q_\zeta}, \quad (\text{C.25})$$

$$\frac{\partial p_s}{\partial \tilde{t}} = \frac{1}{s} \left[ \sum_i \frac{\tilde{p}_i^2}{ms^2} + \frac{\tilde{p}_f^2}{ms^2} + \frac{\tilde{p}_\nu^2}{ms^2} - gk_{\text{B}}T_{\text{K}} \right], \quad (\text{C.26})$$

$$\frac{\partial \nu}{\partial \tilde{t}} = \frac{\tilde{p}_\nu}{Q_\nu s^2}, \quad (\text{C.27})$$

$$\frac{\partial \tilde{p}_\nu}{\partial \tilde{t}} = \mu^1 - \sum_i \phi_{\text{I}}(r_{if}) - \phi_{\text{C}}(\mathbf{r}_f). \quad (\text{C.28})$$

We transform these equations with the relations:  $\tilde{\mathbf{p}}_i/s = \mathbf{p}_i$ ,  $\tilde{\mathbf{p}}_f/s = \mathbf{p}_f$ ,  $\tilde{p}_\nu/s = p_\nu$ ,  $d\tilde{t}/s = dt$ , and thus obtain the canonical equations in the real phase space as

$$\frac{\partial \mathbf{r}_i}{\partial t} = \frac{\mathbf{p}_i}{m}, \quad (\text{C.29})$$

$$\frac{\partial \mathbf{p}_i}{\partial t} = - \sum_{j(\neq i)} \frac{\partial \phi_{\text{I}}(r_{ij})}{\partial \mathbf{r}_i} - \frac{\partial \phi_{\text{C}}(\mathbf{r}_i)}{\partial \mathbf{r}_i} - (\nu - N) \frac{\partial \phi_{\text{I}}(r_{if})}{\partial \mathbf{r}_i} - \mathbf{p}_i \frac{p_s}{Q_\zeta}, \quad (\text{C.30})$$

$$\frac{\partial \mathbf{r}_f}{\partial t} = \frac{\mathbf{p}_f}{m}, \quad (\text{C.31})$$

$$\frac{\partial \mathbf{p}_f}{\partial t} = -(\nu - N) \left[ \sum_i \frac{\partial \phi_{\text{I}}(r_{fi})}{\partial \mathbf{r}_f} - \frac{\partial \phi_{\text{C}}(\mathbf{r}_f)}{\partial \mathbf{r}_f} \right] - \mathbf{p}_f \frac{p_s}{Q_\zeta}, \quad (\text{C.32})$$

$$\frac{\partial s}{\partial t} = s \frac{p_s}{Q_\zeta}, \quad (\text{C.33})$$

$$\frac{\partial p_s}{\partial t} = \sum_i \frac{p_i^2}{m} + \frac{p_f^2}{m} + \frac{p_\nu^2}{m} - gk_{\text{B}}T_{\text{K}}, \quad (\text{C.34})$$

$$\frac{\partial \nu}{\partial t} = \frac{p_\nu}{Q_\nu}, \quad (\text{C.35})$$

$$\frac{\partial p_\nu}{\partial t} = \mu^1 - \sum_i \phi_{\text{I}}(r_{if}) - \phi_{\text{C}}(\mathbf{r}_f) - \frac{p_\nu p_s}{Q_\zeta}. \quad (\text{C.36})$$

From these equations and the transformation  $\zeta = \log s$ , the equations of motion are given by

$$m \frac{d^2 r_i^\alpha}{dt^2} = - \sum_{j(\neq i)} \frac{\partial \phi_{\text{I}}(r_{ij})}{\partial r_i^\alpha} - \frac{\partial \phi_{\text{C}}(\mathbf{r}_i)}{\partial r_i^\alpha} - (\nu - N) \frac{\partial \phi_{\text{I}}(r_{if})}{\partial r_i^\alpha} - m \dot{\zeta} \dot{r}_i^\alpha, \quad (\text{C.37})$$

$$m \frac{d^2 r_f^\alpha}{dt^2} = -(\nu - N) \left[ \sum_i \frac{\partial \phi_{\text{I}}(r_{fi})}{\partial r_f^\alpha} + \frac{\partial \phi_{\text{C}}(\mathbf{r}_f)}{\partial r_f^\alpha} \right] - m \dot{\zeta} \dot{r}_f^\alpha, \quad (\text{C.38})$$

$$Q_\zeta \frac{d^2 \zeta}{dt^2} = 2 \left[ \sum_i \frac{m \dot{r}_i^2}{2} + \frac{m \dot{r}_f^2}{2} + \frac{Q_\nu \dot{\nu}^2}{2} - \frac{g k_B T_{\text{K}}}{2} \right], \quad (\text{C.39})$$

$$Q_\nu \frac{d^2 \nu}{dt^2} = \mu^1 - \sum_i \phi_{\text{I}}(r_{fi}) - \phi_{\text{C}}(\mathbf{r}_f) - Q_\nu \dot{\zeta} \dot{\nu}, \quad (\text{C.40})$$

which do not include to  $\zeta$ . Another difference of the equations of motion between the new and the original GCMD [61] is the presence of the kinetic energy of  $\nu$  in Eq. (C.39), which affects temperature of the system. Therefore, we should select the value of  $Q_\nu$  to be  $Q_\nu \simeq k_B T_{\text{K}} / \langle \dot{\nu}^2 \rangle$ . The derived thermodynamic properties from  $\tilde{H}_{\text{NG}}$  and the grand canonical ensemble average in dynamics described by  $\tilde{H}_{\text{NG}}$  are almost same as those of  $\tilde{H}_{\text{G}}$  [61]. We also apply the MD described by  $\tilde{H}_{\text{NG}}$  to our model, and then obtain conductance similar to that in Fig. 3.1 (a).



# Appendix D

## Conductance under the various parameters

In this appendix, we show the conductance in our MD with changing the chemical-potential difference, the insertion areas of the fractional particles, the electron density, and the strength of the confining potential. Unless otherwise specified, the parameters for the simulations is the same as those for the original in the following (see Sec. 2).

First, we show the conductance for the various differences of the chemical potentials. In Fig. D.1, we plot the calculated conductance  $G$  in our MD simulations for

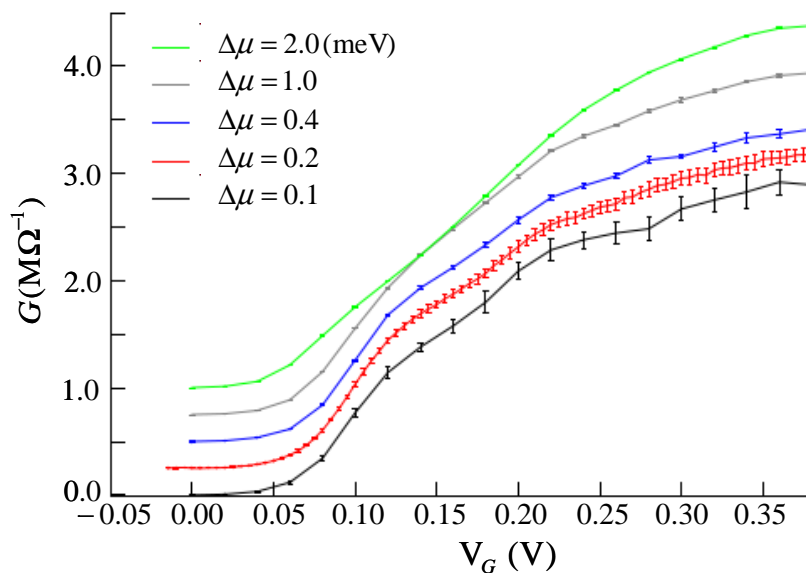


Figure D.1: The DC conductance  $G$  versus the gate voltage  $V_G$  for the chemical-potential differences  $\Delta\mu = 0.1, 0.2, 0.4, 1.0,$  and  $2.0$  meV from bottom to top. Here, the each error bar represents the standard deviation of the ensemble average for each  $G$ .

the chemical-potential differences  $\Delta\mu = 0.1, 0.2, 0.4, 1.0,$  and  $2.0$  meV (see Sec. 2.4). Here,  $G$  is ensemble-averaged over 32 different initial conditions. From Fig. D.1, we can find no steps in the conductance with smaller error bar for each conductance for the higher difference, and the existence of the steps with larger error bars for the lower difference. Because the conductance for  $\Delta\mu = 0.2$  meV is almost identical to those for  $\Delta\mu = 0.1$  and  $0.4$  meV, we verify the linearity of the current in  $\Delta\mu$  for the certain range.

Second, we carry out the MD simulations with changing the insertion areas  $A_L$  and  $A_R$ , under the chemical potentials  $\mu_L = 50.1$  meV and  $\mu_R = 50.0$  meV. We calculate the conductance in the simulations for  $\Delta y = 0.0, 0.1, 0.2, 0.3, 0.4,$  and  $0.5$   $\mu\text{m}$  of the defined areas as

$$\begin{aligned} A_L &= \{(x, y) \mid -(y_{\max} + \Delta y) \leq y \leq -(y_{\min} + \Delta y), |x| \leq x_{\max}\} \\ A_R &= \{(x, y) \mid (y_{\min} + \Delta y) \leq y \leq (y_{\max} + \Delta y), |x| \leq x_{\max}\}, \end{aligned} \quad (\text{D.1})$$

with  $y_{\min} = 31.50$   $\mu\text{m}$ ,  $y_{\max} = y_{\min} + 0.5$   $\mu\text{m}$ , and  $x_{\max} = 7.0$   $\mu\text{m}$  [see Fig. D.2 (a)]. Here, we set  $-y_{\min}$  as the position of the electron present at the furthest left in all of the electrons for the ground-state configuration depicted in Fig. D.2 (a). In Fig. D.2 (b), we plot the conductance  $G$  under the ensemble average over 8 different initial conditions. We can find the larger magnitude of  $G$  as  $\Delta y$  is smaller. This is natural for our system in which the electrons in the reservoirs interact each other. For channel systems connecting two reservoirs, the average current over time in the channel would be determined by the chemical potential at the two boundaries between the channel and the reservoir. Furthermore, the modification of the insertion areas  $A_L$  and  $A_R$  changes the space distribution of the chemical potential in the reservoir. In particular, the shift of  $A_L$  and  $A_R$  to the direction of the channel increases the chemical-potential difference between the two boundaries, which increases the current in the channel. We also confirm the change of the chemical potential distribution with changing  $\Delta y$ , by calculating the chemical potential

$$\hat{\mu}(\mathbf{r}) = k_B T_K \ln [\lambda_D^2 n(\mathbf{r})] + \phi_C(\mathbf{r}) - k_B T_K \ln \left\langle \exp \left[ -\frac{\phi_W(\mathbf{r}, t)}{k_B T_K} \right] \right\rangle, \quad (\text{D.2})$$

which stems from Widom [85–88]. Here,  $n(\mathbf{r})$  is the density distribution function [see Eq. E.1 in Sec. E], and

$$\phi_W(\mathbf{r}, t) = \sum_i \phi_I(|\mathbf{r} - \mathbf{r}_i(t)|) \quad (\text{D.3})$$

is the interaction energy when an electron is hypothetically placed to the position  $\mathbf{r}$ , and then the electron does not actually interact with the other electrons.

Third, we calculate the conductance in the MD simulations under  $V_0 = 0.50$  V for the chemical potential of the right reservoir,  $\mu_R = 50.0, 60.0, 70.0,$  and  $80.0$  meV, where the chemical potential of the left reservoir,  $\mu_L$ , is defined as  $\mu_L = \mu_R + 0.1$  meV. For these chemical potentials, the density in the channel is  $\bar{n} = 2.2, 2.5, 2.9,$  and  $3.4 \times 10^8$   $\text{cm}^{-2}$  from the low to the high chemical potential. For the insertion

areas  $A_L$  and  $A_R$  in this calculations, we adopt Eq. (D.1) with  $y_{\max} = y_{\min} + 0.5 \mu\text{m}$ ,  $\Delta y = 0.35 \mu\text{m}$ , and the obtained  $y_{\min}$  as  $y_{\min} = 30.85, 31.33, 31.71, \text{ and } 31.95 \mu\text{m}$  from the ground-state configuration for  $\mu_L = \mu_R = 50.0, 60.0, 70.0, \text{ and } 80.0 \text{ meV}$ , respectively. In Fig. D.3, we show the conductance  $G$  under the ensemble average over 8 different initial conditions. In this figure,  $G$  for the higher density shifts to the

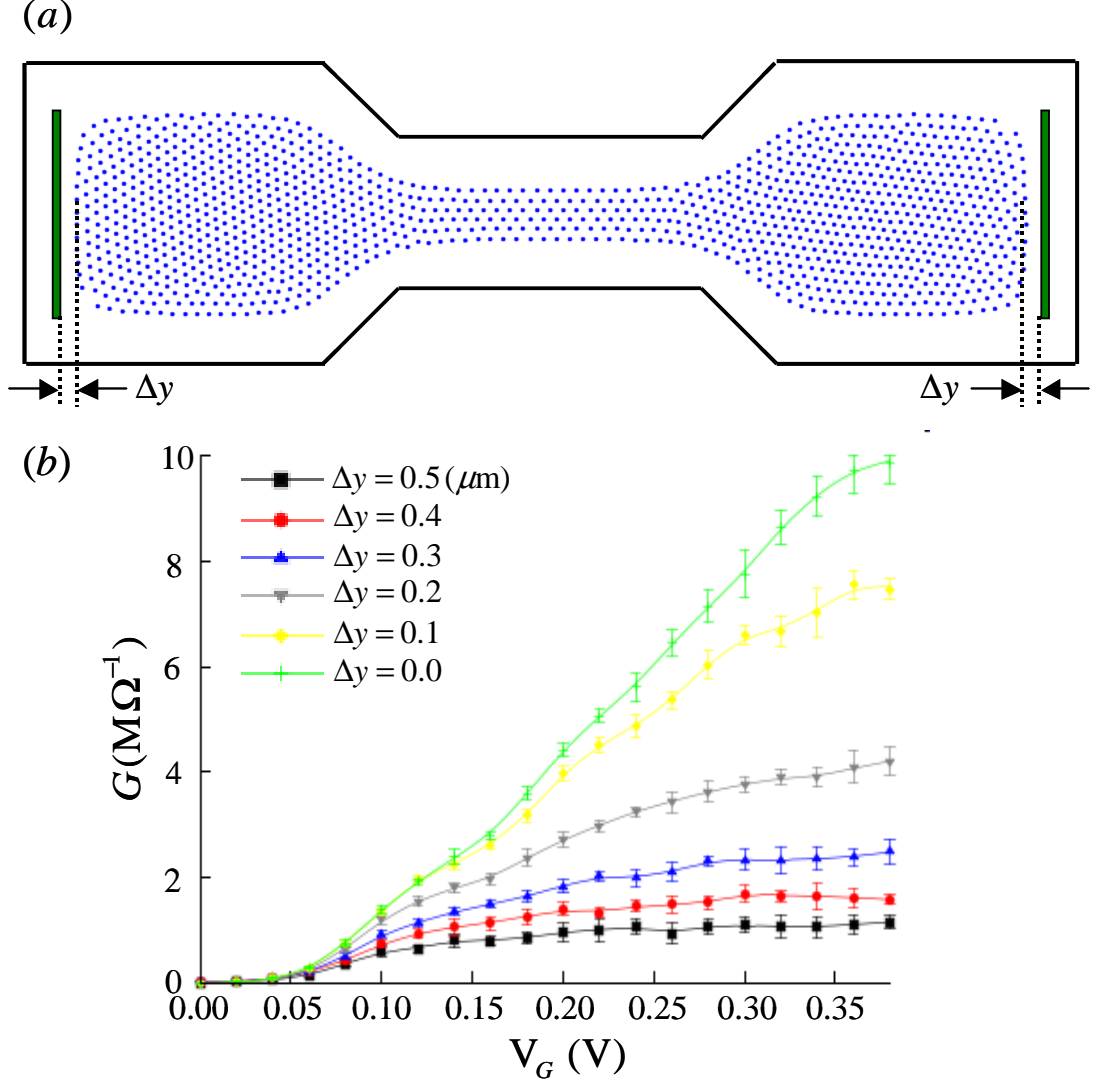


Figure D.2: (a) A schematic diagram for the insertion areas  $A_L$  ( $A_R$ ) of the fractional particle in the left (right) reservoir (green areas). Here,  $\Delta y$  is the separation from the edge of  $A_L$  ( $A_R$ ) to the position of the electron present at the furthest left (right) in all of the electrons. The blue circles indicate the position of electrons in the ground-state configuration for  $\mu_L = \mu_R = 50.00 \text{ meV}$ . (b) The DC conductance  $G$  versus the gate voltage  $V_G$  for  $\Delta y = 0.0, 0.1, 0.2, 0.3, 0.4, \text{ and } 0.5 \mu\text{m}$  from top to bottom. Here, the each error bar represents the standard deviation of the ensemble average for each  $G$ .

lower  $V_G$  direction. This is because the potential energy of the electrons for higher density exceeds the higher potential barrier in the gate (see Sec. 3).

Fourth, we show the conductance for the reservoir voltage  $V_0 = 0.4, 0.5, 0.6,$  and  $0.7$  V, under the chemical potentials  $\mu_L = 70.1$  meV and  $\mu_R = 70.0$  meV. For the insertion areas  $A_L$  and  $A_R$  in this simulations, we adopt Eq. (D.1) with  $y_{\max} = y_{\min} + 0.5 \mu\text{m}$ ,  $\Delta y = 0.35 \mu\text{m}$ , and the obtained  $y_{\min}$  as  $y_{\min} = 32.17, 31.71, 31.32,$  and  $30.90 \mu\text{m}$  from the ground-state configuration under  $\mu_L = \mu_R = 70.0$  meV for  $V_0 = 0.4, 0.5, 0.6,$  and  $0.7$  V, respectively. In Fig. D.4, we plot the conductance  $G$  under the ensemble average over 8 different initial conditions. The conductance  $G$  for these voltages shifts to the higher  $V_G$  direction as  $V_0$  is higher. This shift is because the strength of the point contact is almost determined by the electric potential difference  $V_0 - V_G$ .

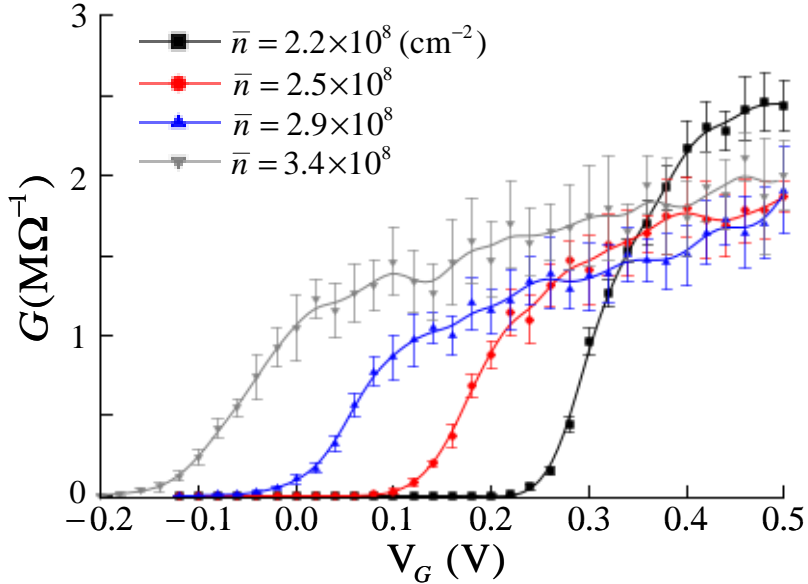


Figure D.3: The DC conductance  $G$  versus the gate voltage  $V_G$  under  $V_0 = 0.50$  V for the channel density  $\bar{n} = 2.2, 2.5, 2.9,$  and  $3.4 \times 10^8 \text{ cm}^{-2}$  from right to left. Here, the each error bar represents the standard deviation of the ensemble average for each  $G$ .

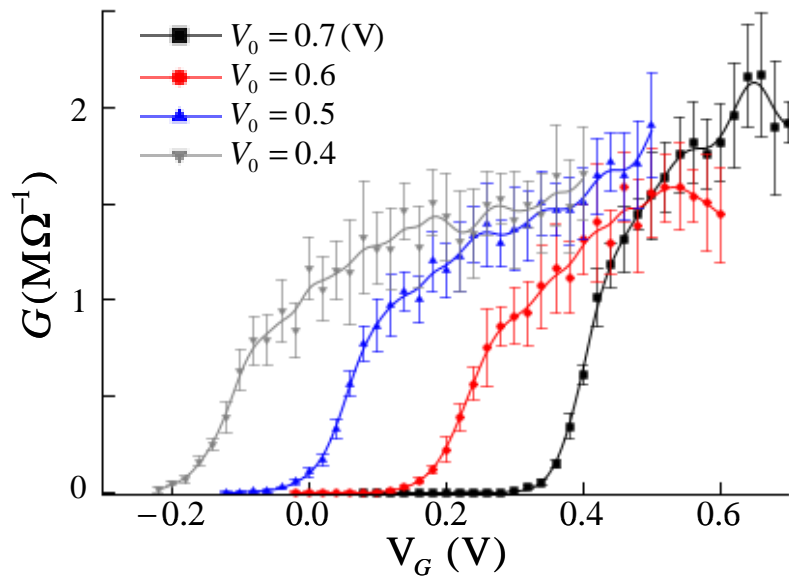


Figure D.4: The DC conductance  $G$  versus the gate voltage  $V_G$  for the reservoir voltage  $V_0 = 0.4, 0.5, 0.6,$  and  $0.7$  V from left to right. Here, the each error bar represents the standard deviation of the ensemble average for each  $G$ .



# Appendix E

## Calculation method of physical quantities

The one-particle quantities we calculate are the density distribution function averaged over the  $0.1 \mu\text{m}$  square  $\delta\mathbf{r}$  centered around the position  $\mathbf{r}$ :

$$n(\mathbf{r}) = \left\langle \sum_i \delta(\mathbf{r} - \mathbf{r}_i(t)) \right\rangle, \quad (\text{E.1})$$

the average potential energy of electrons in  $\delta\mathbf{r}$ ,

$$\Phi(\mathbf{r}) = \langle \phi(\mathbf{r}_i, t) | (\delta\mathbf{r})_1 \rangle, \quad (\text{E.2})$$

the standard deviation of temporal fluctuation of  $\Phi(\mathbf{r})$ ,

$$\sigma(\mathbf{r}) = \left\{ \left\langle |\phi(\mathbf{r}_i, t) - \Phi[\mathbf{r}_i(t)]|^2 \middle| (\delta\mathbf{r})_1 \right\rangle \right\}^{\frac{1}{2}}, \quad (\text{E.3})$$

and the root mean square (RMS) of the electric field,

$$F(\mathbf{r}) = \left\{ \left\langle |\nabla_i \phi(\mathbf{r}_i, t)|^2 \middle| (\delta\mathbf{r})_1 \right\rangle \right\}^{\frac{1}{2}}, \quad (\text{E.4})$$

where  $\langle \dots | (\delta\mathbf{r})_1 \rangle$  represents the ensemble average under a conditional time average for electrons in  $\delta\mathbf{r}$ , when electrons are present in  $\delta\mathbf{r}$ . Here,  $\delta\mathbf{r}$  is created by dividing the  $xy$  plane into  $0.1 \mu\text{m}$  square mesh, and  $n$  in  $(\delta\mathbf{r})_n$  denotes that the averaged quantity is the  $n$ -particle quantity. The conditional time average is defined by

$$\frac{1}{t_{\text{P}}(\delta\mathbf{r})} \int_0^{t_{\text{T}}} dt \int_{\delta\mathbf{r}} d^2\mathbf{r}' \sum_i \delta[\mathbf{r}' - \mathbf{r}_i(t)] \dots,$$

where  $t_{\text{T}}$  is the calculation time, and

$$t_{\text{P}}(\delta\mathbf{r}) \equiv \int_0^{t_{\text{T}}} dt \int_{\delta\mathbf{r}} d^2\mathbf{r}'' \sum_k \delta[\mathbf{r}'' - \mathbf{r}_k(t)]$$

is the total presence time of electrons in  $\delta\mathbf{r}$ . We also confirm that the quantities are almost in agreement with those calculated with  $\delta\mathbf{r}$  to be  $0.05 \mu\text{m}$  squares. In addition, we use another conditional average for a two-particle quantity as follows:

$$\langle \cdots | (S)_2^m \rangle = \left\langle \frac{1}{t_{2\text{P}}(S; m)} \int_0^{t_{\text{T}}} dt \delta(m - N_S(t)) \int_S d^2\mathbf{r}' \int_S d^2\mathbf{r}'' \sum_{i>j} \delta[\mathbf{r}' - \mathbf{r}_i(t)] \delta[\mathbf{r}'' - \mathbf{r}_j(t)] \cdots \right\rangle_{\text{E}}, \quad (\text{E.5})$$

where  $\langle \cdots \rangle_{\text{E}}$  is the ensemble average,  $N_S(t)$  is the number of electrons in an area  $S$  at time  $t$ :

$$N_S(t) = \int_S d^2\mathbf{r}' \sum_k \delta[\mathbf{r}' - \mathbf{r}_k(t)],$$

and  $t_{2\text{P}}(S; m)$  is the product of the number of pairs among  $m$  electrons and the presence time when just  $m$  electrons are present in  $S$ ,

$$t_{2\text{P}}(S; m) = \int_0^{t_{\text{T}}} dt \delta[m - N_S(t)] \int_S d^2\mathbf{r}' \int_S d^2\mathbf{r}'' \sum_{k>l} \delta[\mathbf{r}' - \mathbf{r}_k(t)] \delta[\mathbf{r}'' - \mathbf{r}_l(t)].$$

Thus,  $\langle \cdots | (S)_2^m \rangle$  describes the ensemble and the conditional time averages, among  $m$  electrons in  $S$ , when just  $m$  electrons are present in  $S$ . Incidentally, all of the introduced quantities in this chapter are time and ensemble averaged over 1,200,000 time steps and 32 different initial conditions, respectively.

# Appendix F

## Fluctuation properties

In this appendix, we first show the distribution of temporal variation of electric potential, to demonstrate that the Gaussian approximation in Sec. 4.1 is appropriate. Next, we compare the calculated electric field in our MD with one of the previous studies [64].

In Fig. F.1, we compare the directly calculated potential distribution in terms of the MD simulation with the normal distribution with the calculated standard

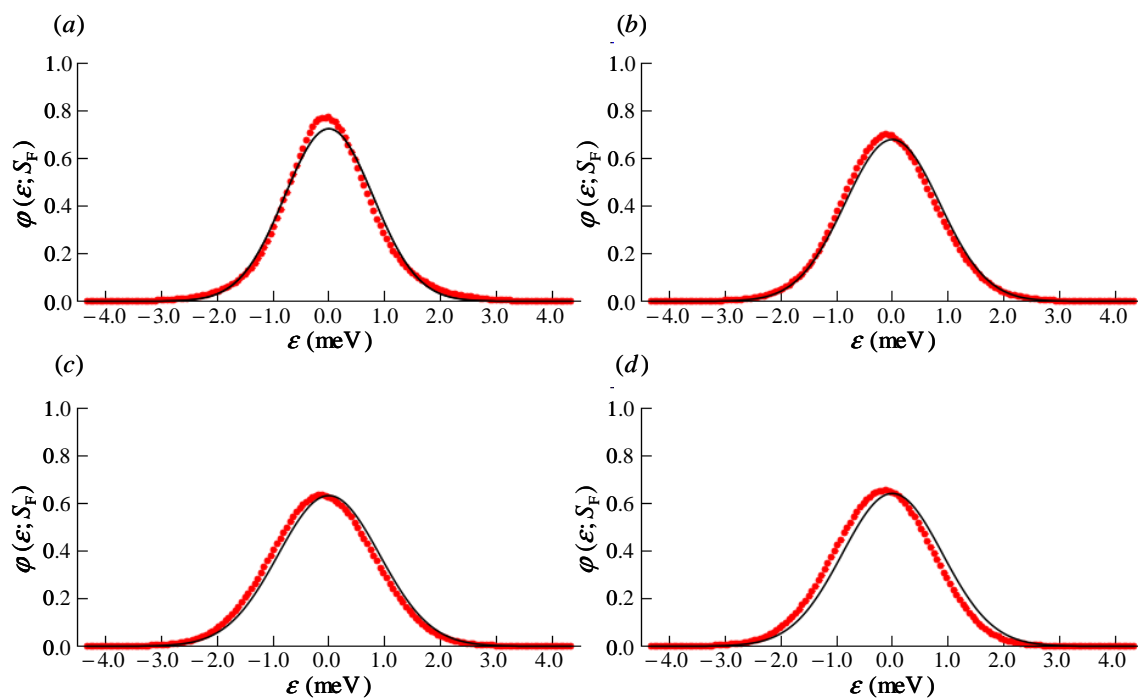


Figure F.1: The potential distributions  $\varphi(\epsilon; S_F)$  (red circles), and the normal distributions with  $\sigma_F$  as the standard deviation (black line), at (a)  $V_G = 0.05$  V, (b)  $V_G = 0.10$  V, (c)  $V_G = 0.15$  V, and (d)  $V_G = 0.28$  V.

deviation. The potential distribution is calculated with the following equations;

$$\varphi(\epsilon; \mathbf{r}) = \langle \delta [\epsilon - \{\phi(\mathbf{r}_i, t) - \Phi(\mathbf{r}_i(t))\}] |(\delta \mathbf{r})_1 \rangle, \quad (\text{F.1})$$

and

$$\varphi(\epsilon; S_F) = \int_{S_F} d^2 \mathbf{r} f(\epsilon; S_F) \varphi(\epsilon; \mathbf{r}), \quad (\text{F.2})$$

where  $\langle \dots |(\delta \mathbf{r})_1 \rangle$  and  $\Phi$  in Eq. (F.1) are introduced in Appendix E, and  $S_F$  and  $f(\epsilon; S_F)$  in Eq. (F.2) are defined in Eq. 3.1. The normal distribution with the standard deviation  $\sigma_F$  in Fig. 3.3 is given by

$$\frac{1}{\sqrt{2\pi\sigma_F^2}} \exp \left[ -\frac{\epsilon^2}{2\sigma_F^2} \right]. \quad (\text{F.3})$$

From Fig. F.1, we believe that the Gaussian approximation for the potential distribution in Sec. 4.1 is quite reasonable.

We next demonstrate that our simulation semi-quantitatively reproduces temporal fluctuation of the electric field which occurs from density fluctuation [64], as with the potential fluctuation. In Ref. [64], the fluctuational field for classical 2D electrons interacting through the bare Coulomb potential is introduced as

$$F_C = \sqrt{\langle |\mathbf{F}_C|^2 \rangle} = \sqrt{\Xi_C(\Gamma) n_s^{3/2} k_B T} \quad (\text{F.4})$$

with the numerical factor  $\Xi_C(\Gamma)$

$$\Xi_C(\Gamma) = \int d^2(\mathbf{r}n_s) \frac{\tilde{g}(rn_s^{1/2}; \Gamma)}{(rn_s^{1/2})^3},$$

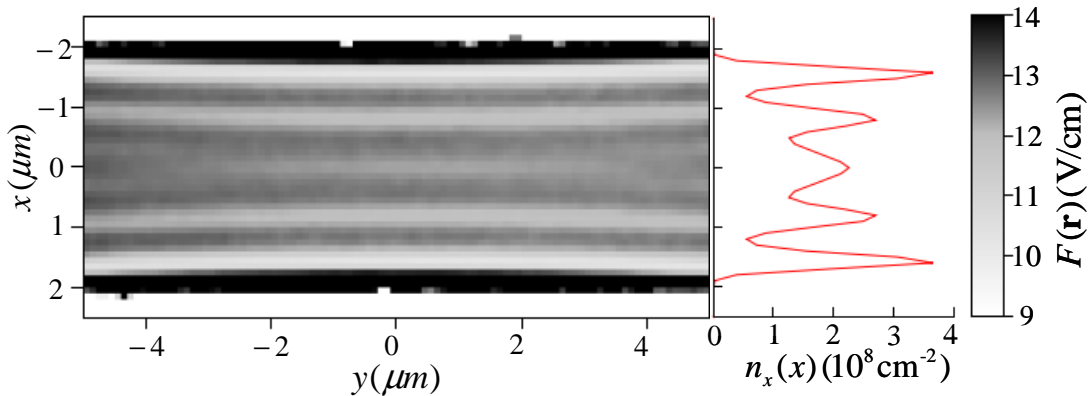


Figure F.2: The RMS of electric field  $F(\mathbf{r})$  in the region of  $|y| \leq 5 \mu\text{m}$  in the channel at  $V_G = 0.38 \text{ V}$ . The curve at the right of the field distribution shows the averaged density profile across the channel,  $n_x(x) = \frac{1}{L} \int_{-L/2}^{L/2} dy n(\mathbf{r})$  with  $L = 10.0 \mu\text{m}$ .

where  $\tilde{g}(rn_s^{1/2}; \Gamma)$  is the pair correlation function of the inter-electron distance scaled by  $n_s^{-1/2}$ . They examined the above expressions by Monte Carlo simulations in extensive plasma parameters in the range of  $10 < \Gamma < 200$ . To simplify the comparison between the fluctuation in our MD and Eq. (F.4), we investigate the electric field in the region of  $|y| \leq 5 \mu\text{m}$  without the point contact, where the calculated density from the inter-electron separation  $\bar{r} = 0.809 \mu\text{m}$  in the region is  $1.94 \times 10^8 \text{cm}^{-2}$ .

Under the density,  $\Gamma$ , and  $T_K$ , Eq. (F.4) yields  $F_C = 19.5 \text{ V/cm}$ . On the other hand, the directly calculated electric field with Eq. (E.4) in our simulations is given by

$$\bar{F} = \int_{|y| < 5\mu\text{m}} d^2\mathbf{r} f(\mathbf{r}; |y| < 5\mu\text{m}) F(\mathbf{r}) \approx 11.9 \text{ V/cm}, \quad (\text{F.5})$$

where the normalized distribution function  $f(\mathbf{r}; |y| < 5\mu\text{m})$  is introduced in Eq. (3.2). The difference  $7.6 \text{ V/cm}$  originates partially in the screening effects for our system, and the existence of edges in the channel. First, we estimate the ratio of the electric field in our system to the bare Coulomb field, in the approximation that the pair correlation function is the step function of  $|\mathbf{r}| - \bar{r}$ . The ratio is given by

$$\frac{\sqrt{\int_0^\infty dr r \theta(r - \bar{r}) |\nabla \phi_I(r)|^2}}{\sqrt{\int_0^\infty dr r \theta(r - \bar{r}) |\nabla \frac{1}{r}|^2}} \approx 0.906. \quad (\text{F.6})$$

where the step function  $\theta$  is introduced in Eq. (2.7). Therefore,  $F_C$  may reduce to  $0.906 \times F_C = 17.7 \text{ V/cm}$  as the screening exists. We next consider the reduction of electric field of the electrons at the edges. Electrons along the edges are surrounded by four electrons against interior electrons with the six neighboring electrons on average. Because of the dominant contribution of the neighboring electrons on the fluctuational field [69], the edge electrons ought to have two third times as strong fluctuational field as the interior electrons have. This is reasonably confirmed from  $F(\mathbf{r})$  and  $n(\mathbf{r})$ , depicted in Fig. F.2. In addition, it is found from the figure that electrons in the channel are organized into five high-density lines. From this discussion, the value of  $F_C$  in the channel should be  $\{(3/5) + (2/5) \times (2/3)\} \times 0.906 \times F_C = 15.3 \text{ V/cm}$  whose difference from  $\bar{F}$  is about 20 percent. Therefore, we expect that fluctuation dynamics of electrons in our system is consistent with that of the previous studies and thus the potential fluctuation shows valid values.



# Bibliography

- [1] C. W. J. Beenakker, and H. van Houten, *Solid State Phys.* **44**, 1 (1991).
- [2] F. A. Buot, *Phys. Rep.* **234**, 73 (1993).
- [3] N. Agraït, A. L. Yeyati, and J. M. van Ruitenbeek, *Phys. Rep.* **377**, 81 (2003).
- [4] S. Datta, *Electronic Transport in Mesoscopic Systems* (Cambridge University Press, Cambridge, 1995).
- [5] A. G. M. Jansen, A. P. van Gelder, and P. Wyder, *J. Phys. C: Solid State Phys.* **13** 6073, (1980).
- [6] A. M. Duif, and A. G. M. Jansen, and P. Wyder, *J. Phys.: Condens. Matter* **1**, 3157 (1989).
- [7] Yu. G. Naidyuk, and I. K. Yansen, *J. Phys.: Condens. Matter* **10**, 8905 (1998).
- [8] D. Daghero, and R. S. Gonnelli, *Supercond. Sci. Technol.* **23**, 043001 (2010).
- [9] G. Wexler, *Proc. Phys. Soc. London*, **89**, 927 (1966).
- [10] M. J. M. de Jong, *Phys. Rev. B*, **49**, 7778 (1994).
- [11] B. Nikolić, and P. B. Allen, *Phys. Rev. B*, **60**, 3963 (1999).
- [12] J. C. Maxwell, *A Treatise on Electricity and Magnetism* (Dover, New York, 1891).
- [13] Yu. V. Sharvin, *Zh. Eksp. Teor. Fiz.* **48**, 984 (1965) [*Sov. Phys. JETP* **21**, 655 (1965)].
- [14] S. Tarucha, T. Saku, Y. Tokura, and Y. Hirayama, *Phys. Rev. B*, **47**, 4064 (1993).
- [15] A. Halbritter, L. Borda, and A. Zawadowski, *Adv. Phys.* **53**, 939 (2004).
- [16] B. J. van Wees, H. van Houten, C. W. J. Beenakker, J. G. Williamson, L. P. Kouwenhoven, D. van der Marel, and C. T. Foxon, *Phys. Rev. Lett.* **60**, 848 (1988).

- [17] M. Yosefin, and M. Kaveh, Phys. Rev. Lett. **64**, 2819 (1990).
- [18] J. E. Black, Phys. Rev. B, **21**, 3279 (1980).
- [19] L. W. Molenkamp, and M. J. M. de Jong, Phys. Rev. B, **49**, 5038 (1994).
- [20] M. J. M. de Jong, and L. W. Molenkamp, Phys. Rev. B, **51**, 13389 (1995).
- [21] R. N. Gurzhi, A. N. Kalinenko, and A. I. Kopeliovich, Phys. Rev. Lett, **74**, 3872 (1995).
- [22] K. E. Nagaev, and O. S. Ayavazyan, Phys. Rev. Lett, **101**, 216807 (2008).
- [23] M. Köppl, P. Henseler, A. Erbe, P. Nielaba, and P. Leiderer, Phys. Rev. Lett. **97**, 208302 (2006).
- [24] P. Henseler, A. Erbe, M. Köppl, P. Leiderer, and P. Nielaba, Phys. Rev. E. **81**, 041402 (2010).
- [25] G. Piacente and F. M. Peeters, Phys. Rev. B, **72**, 205208 (2005).
- [26] G. Goel, W. P. Krekelberg, J. R. Errington, and T. M. Truskett, Phys. Rev. Lett. **100**, 106001 (2008).
- [27] J. Mittal, T. M. Truskett, J. R. Errington, and G. Hummer, Phys. Rev. Lett. **100**, 145901 (2008).
- [28] P. Glasson, V. Dotsenko, P. Fozooni, M. J. Lea, W. Bailey, G. Papageorgiou, S. E. Andresen, and A. Kristensen, Phys. Rev. Lett. **87**, 176802 (2001).
- [29] Y. Monarkha and K. Kono, *Two-Dimensional Coulomb Liquids and Solids* (Springer-Verlag, Berlin, 2004).
- [30] Yu. Z. Kovdrya, J. Low Temp. Phys. **29**, 77 (2003).
- [31] D. G. Rees, I. Kuroda, C. A. Marrache-Kikuchi, M. Höfer, P. Leiderer, and K. Kono, Phys. Rev. Lett, **106**, 026803 (2011).
- [32] C. Nakajima, and H. Hayakawa, Prog. Theor. Phys. **122**, 1377 (2009). See also C. Nakajima, PhD Thesis, Kyoto University (2010).
- [33] H. Ikegami, H. Akimoto, and K. Kono, Phys. Rev. B, **82**, 201104(R) (2010).
- [34] H. Ikegami, H. Akimoto and K. Kono, Phys. Rev. Lett, **102**, 046807 (2009).
- [35] V. B. Shikin and Yu. P. Monarkha, J. Low Temp. Phys. **15**, 193 (1974).
- [36] S. S. Sokolov J. Low Temp. Phys. **30**, 199 (2004).
- [37] D. Coimbra, S. S. Sokolov, J. P. Rino, and N. Studart, J. Low Temp. Phys. **126**, 505 (2002).

- [38] S. S. Sokolov and N. Studart, Phys. Rev. B. **67**, 132510 (2003).
- [39] S. S. Sokolov, N. Studart, and D. Coimbra, J. Low. Temp. Phys. **138**, 409 (2005).
- [40] D. Coimbra, S. S. Sokolov, J.-P. Rino, and N. Studart, Phys. Rev. B. **74**, 035411 (2006).
- [41] M. Saitoh, J. Phys. Soc. Jpn. **42**, 201 (1977).
- [42] V. A. Buntar', Yu. Z. Kovdrya, V. N. Grigor'ev, Yu. P. Monarkha, and S. S. Sokolov, Fiz. Nizk. Temp. **13**, 789 (1987) [Sov. J. Low Temp. Phys. **13**, 451 (1987)].
- [43] Yu. G. Gurevich, and O. L. Mashkevich, Phys. Rep. **181**, 327 (1989).
- [44] V. A. Buntar', V. N. Grigoriev, O. I. Kirichuk, Yu. Z. Kovdrya, Yu. P. Monarkha, and S. S. Sokolov, J. Low Temp. Phys. **79**, 323 (1990).
- [45] V. A. Buntar and S. S. Sokolov, Fiz. Nizk. Temp. **16**, 845 (1990) [Sov. J. Low Temp. Phys. **16**, 497 (1990)].
- [46] K. A. Nasyedkin, V. E. Sivokon, Yu. P. Monarkha, and S. S. Sokolov, J. Low Temp. Phys. **35**, 757 (2009).
- [47] Yu. M. Vil'k, and Yu. P. Monarkha, Fiz. Nizk. Temp. **15**, 235 (1989) [Sov. J. Low Temp. Phys. **15**, 131 (1989)].
- [48] V. Syvokon, Y. Monarkha, K. Nasyedkin, and S. Sokolov, J. Low Temp. Phys. **148**, 169 (2007).
- [49] E. Y. Andrei, *2D Electron Systems on Helium and Other Substrates* (Kluwer Academic, New York, 1997).
- [50] M. I. Dykman, C. Fang-Yen, and M. J. Lea, Phys. Rev. B **55**, 16249 (1997).
- [51] M. Araki and H. Hayakawa, Phys. Rev. B **86**, 165412 (2012).
- [52] P. M. Morse and H. Feshbach, *Methods of Theoretical Physics(Part I)*, (McGraw-Hill, New York, 1953).
- [53] W. R. Smythe, *Static and Dynamic Electricity*, (McGraw-Hill, New York, 1953).
- [54] F. M. Peeters, Phys. Rev. B. **30**, 159 (1984).
- [55] S. Nosé, J. Chem. Phys. **81**, 511 (1984).
- [56] W. G. Hoover, Phys. Rev. A **31**, 1695 (1985).
- [57] S. Nosé, Prog. Theor. Phys. Supplement No. **103**, 1 (1991).

- [58] T. Cagin and M. Pettitt, *Molecular Simulation* **6**, pp. 5-26(1991).
- [59] T. Cagin and M. Pettitt, *Molecular Physics*, **72**, No. 1, 169-175(1991).
- [60] S. Weerasinghe and M. Pettitt, *Molecular Physics*, **82**, No. 5, 897-912(1994).
- [61] G. C. Lynch and M. Pettitt, *J. Chem. Phys.* **107**, 8594 (1997).
- [62] J. P. Hansen and I. R. McDonald, *Theory of Simple Liquids, 3rd Ed.*, (Academic Press Netherlands, 2006).
- [63] B. L. Holian, A. F. Voter and R. Ravelo, *Phys. Rev. E* **52**, 2338 (1995).
- [64] C. Fang-Yen and M. I. Dykman, and M. J. Lea, *Phys. Rev. B*, **55**, 16272 (1997).
- [65] M. Saitoh, *Phys. Rev. B*. **40**, 810 (1989).
- [66] C. C. Grimes and G. Adams, *Phys. Rev. Lett.* **42**, 795 (1979).
- [67] K.-A. Liu and Lin I., *Phys. Rev. E*, **82**, 041504 (2010).
- [68] G. Piacente, I. V. Schweigert, J. J. Betouras, and F. M. Peeters, *Phys. Rev. B*, **69**, 045324 (2004).
- [69] M. I. Dykman, and L. P. Pryadko, *Phys. Rev. B*, **67**, 235104 (2003).
- [70] D. G. Rees, H. Totsuji, and K. Kono, *Phys. Rev. Lett*, **108**, 176801 (2012).
- [71] M. C. Wang and G. E. Uhlenbeck, *Rev. mod. Phys.*, **17**, 323 (1945).
- [72] M. W. Cole, and M. H. Cohen, *Phys. Rev. Lett.* **23**, 1238 (1969).
- [73] W. T. Sommer, *Phys. Rev. Lett.* **12**, 271 (1964).
- [74] Milton W. Cole, *Phys. Rev. B* **3**, 4418 (1971).
- [75] Hua Wu, D W L Sprung, and J Martorell, *Eur. J. Phys.* **21**, 413 (2000).
- [76] M. A. Woolf, and G. W. Rayfield, *Phys. Rev. Lett.* **15**, 235 (1965).
- [77] Sviatoslav S Sokolov, and Nelson Studart, *J. Phys.: Condens. Matter* **12**, 9563 (2000).
- [78] C. L. Zipfel, T. R. Brown, and C. C. Grimes, *Phys. Rev. Lett.* **37**, 1760 (1976).
- [79] K. Fuchs, *Proc. Cambridge Philos. Soc.* **34**, 100 (1938).
- [80] E. H. Sondheimer, *Adv. Phys.* **1**, 1 (1952).
- [81] D. K. C. MacDonald and K. Sarginson, *Proc. R. Soc. London, Ser. A* **203**, 223 (1950).

- [82] R. B. Dingle, Proc. R. Soc. London, Ser. A **201**, 545 (1950).
- [83] R. G. Chambers, Proc. R. Soc. London, Ser. A **202**, 375 (1950).
- [84] C. W. J. Beenakker, and H. van Houten, Phys. Rev. B, **38**, 3232 (1988).
- [85] B. Widom, J. Chem. Phys. **39**, 2808 (1963).
- [86] B. Widom, J. Stat. Phys. **19**, 563 (1978).
- [87] J. G. Powles, S. E. Baker and W. A. B. Evans, J. Chem. Phys. **101**, 4098 (1994).
- [88] J. G. Powles, B. Holtz and W. A. B. Evans, J. Chem. Phys. **101**, 7804 (1994).
- [89] M. P. Allen and D. J. Tildesley, *Computer Simulatin of Liquids*, (Oxford University Press, New York, 1987).
- [90] DL Ermak and H. Buckholz, J. Comput. Phys., **35**, 169 (1980).
- [91] S. Chandrasekhar, Rev. mod. Phys., **15**, 1 (1943).